

## Article

# From Sub-Solar to Super-Solar Chemical Abundances along the Quasar Main Sequence

Paola Marziani <sup>1,\*</sup>, Alberto Floris <sup>2</sup>, Alice Deconto-Machado <sup>3</sup>, Swayamtrupta Panda <sup>4</sup>, Marzena Sniegowska <sup>5</sup>, Karla Garnica <sup>6</sup>, Deborah Dultzin <sup>6</sup>, Mauro D'Onofrio <sup>1,2</sup>, Ascensión Del Olmo <sup>3</sup>, Edi Bon <sup>7</sup> and Nataša Bon <sup>7</sup>

- <sup>1</sup> National Institute for Astrophysics (INAF), Astronomical Observatory of Padova, IT-35122 Padova, Italy; mauro.donofrio@unipd.it
- <sup>2</sup> Department of Physics and Astronomy, University of Padua, Vicolo dell' Osservatorio 3, IT-35122 Padova, Italy; alberto.floris@studenti.unipd.it
- <sup>3</sup> Instituto de Astrofísica de Andalucía, Consejo Superior de Investigaciones Científicas (IAA-CSIC), Glorieta de Astronomía s/n, 18008 Granada, Spain; adeconto@iaa.es (A.D.-M.); chony@iaa.es (A.D.O.)
- <sup>4</sup> Laboratório Nacional de Astrofísica, Ministério da Ciência, Tecnologia e Inovação (MCTI), R. dos Estados Unidos 154, Nações, Itajubá CEP 37504-364, Brazil; spanda@lna.br
- <sup>5</sup> School of Physics and Astronomy, Tel Aviv University, Tel Aviv 69978, Israel; msniegowska@camk.edu.pl
- <sup>6</sup> Institute of Astronomy, National Autonomous University of Mexico (UNAM), Mexico City 04510, Mexico; kgarnica@astro.unam.mx (K.G.); deborah@astro.unam.mx (D.D.)
- <sup>7</sup> Belgrade Astronomical Observatory, Volgina 7, 11000 Belgrade, Serbia; ebon@aob.rs (E.B.); nbon@aob.rs (N.B.)
- \* Correspondence: paola.marziani@inaf.it

**Abstract:** The 4D (four-dimensional) eigenvector 1 (E1) sequence has proven to be a highly effective tool for organizing observational and physical properties of type-1 active galactic nuclei (AGNs). In this paper, we present multiple measurements of metallicity for the broad line region gas, from new and previously-published data. We demonstrate a consistent trend along the optical plane of the E1 (also known as the quasar main sequence), defined by the line width of Balmer hydrogen H $\beta$  profile and by a parameter measuring the prominence of singly-ionized iron emission. The trend involves an increase from sub-solar metallicity in correspondence with extreme Population B (weak FeII emission, large H $\beta$  FWHM (full width at half maximum)) to metallicity several tens the solar value in correspondence with extreme Population A (strongest FeII optical emission, narrower H $\beta$  profiles). The data establish the metallicity as a correlate of the 4DE1/main sequence. If the considerably high metallicity ( $Z \gtrsim 10Z_{\odot}$ , solar metallicity) gas is expelled from the sphere of influence of the central black hole, as indicated by the widespread evidence of nuclear outflows and disk wind in the case of sources radiating at a high Eddington ratio, then it is possible that the outflows from quasars played a role in chemically enriching the host galaxy.

**Keywords:** active galactic nuclei; optical spectroscopy; ionized gas; broad line region; interstellar medium; chemical composition; quasar main sequence; photo-ionization



**Citation:** Marziani, P.; Floris, A.; Deconto-Machado, A.; Panda, S.; Sniegowska, M.; Garnica, K.; Dultzin, D.; D'Onofrio, M.; Del Olmo, A.; Bon, E.; et al. From Sub-Solar to Super-Solar Chemical Abundances along the Quasar Main Sequence. *Physics* **2024**, *6*, 216–236. <https://doi.org/10.3390/physics6010016>

Received: 7 November 2023

Revised: 4 January 2024

Accepted: 9 January 2024

Published: 17 February 2024



**Copyright:** © 2024 by the authors. Licensee MDPI, Basel, Switzerland. This article is an open access article distributed under the terms and conditions of the Creative Commons Attribution (CC BY) license (<https://creativecommons.org/licenses/by/4.0/>).

## 1. Introduction: A Main Sequence and the Eigenvector 1 for Quasars

The main sequence (MS) concept in quasar research draws parallels with stellar evolutionary sequences, but in this case, it is applied to quasar properties. A study on a sample of Palomar-Green quasars detected an interesting anti-correlation between the strength of the FeII $\lambda$ 4570 emission blend and the full width at half maximum (FWHM) of the broad Balmer hydrogen H $\beta$  emission line of type-1 quasars with low redshifts ( $z < 1$ ) [1]. This anti-correlation suggests that, as the FeII $\lambda$ 4570 feature becomes stronger, the FWHM tends to decrease, and is one of the main correlations known as the eigenvector 1 of quasars. This finding has been established through the analysis of samples of increasing size over the years [2–5], and has proved to be fundamental to organize type-1 active galactic nuclei (AGNs) properties in a systematic way with predictive ability.

Quasars are categorized into different spectral types along the MS (e.g., [5]) and two primary populations, referred to as Population A (Pop. A) and Population B (Pop. B), have been identified [3]. These categories are based on specific properties such as the Eddington ratio (a measure of the accretion rate per unit black hole mass) and orientation [5–7]. The “4DE1” classification, introduced in Ref. [3], further organizes quasar properties according to the Eddington ratio and orientation, revealing a systematic pattern of variation across different types of AGN encompassing their outflow phenomenology and their accretion mode [8]. The assignment of most quasar spectral types permitted the prediction of their UV (ultraviolet), X-ray, radio, and FIR (far-infrared) properties with a high degree of confidence.

The MS, quite similar to the equivalent concept in stellar evolution, is used as an evolutionary framework for understanding quasars. This sequence spans from young and rejuvenated quasars, characterized by specific spectral properties (extreme Population A, xA), to older and more mature quasars with distinct characteristics (Pop. B). Differences in factors such as black hole mass, Eddington ratio, disk winds, or outflow properties, derived from the strengths and profiles of emission lines are used to define and distinguish these evolutionary stages [9,10].

Currently, the available evidence regarding the correlation between metal content in the broad line emitting region (BLR) and the quasar MS remains partial and inconclusive [7,11]. There is a long tradition of studies attempting to estimate the metallicity in the BLR of AGNs over a broad range of redshifts, from  $z \approx 0$  to  $z \approx 6$  (e.g., [12–18]). All these studies derive metallicity in the range from a few to about 10 times solar metallicity ( $Z_{\odot}$ ) values that are significantly higher than the ones found even in most massive and metal-rich galaxies [19,20]. When considering the past metallicity estimates along the main sequence, an intriguing differentiation emerges: not all quasars are accreting matter with super-solar metal content [21], and only at one end of the MS, the BLR gas may be enriched by a metal content even above ten times solar, possibly with pollution by supernova ejecta [22].

In this paper, we use the results of a new analysis and of several recent papers to gather a view of the global trend along the MS. Section 2 summarizes the new observations from ground- and space-based observatories. Section 3 elucidates the methodology applied to the metallicity estimates, stressing the need to isolate line components that are spectroscopically resolved, and may correspond to emitting regions in different physical conditions (Section 3.1). Results of several individual sources and composite spectra representative of entire spectral types (STs) introduced in Section 4 delineate a sequence of increasing metallicity from extreme Pop. B to extreme Pop. A (Section 5). As soon as the outflows from the AGNs are of special relevance for galactic evolution [23–25], it is essential to isolate the corresponding line component, whenever possible (Section 5.3). The AGN outflows can provide enrichment of the nuclear and circumnuclear region of the host galaxies (Section 6), although ensuing chemical feedback is expected to be relevant only at high AGN luminosity. In Section 6, we outline how the different metallicities inferred for the BLR of low- $z$  AGNs fit the evolutionary interpretation of the quasar MS.

## 2. Observations

The new spectral data employed in this study were acquired through a series of distinct observations. Specifically:

- For Mrk (Markarian) 335, Mrk 478, and Fairall 9, we utilized optical spectra sourced from Ref. [26]. Additionally, the UV spectra of Mrk 335 were obtained during observations conducted on the 4 and 7 January 2013, utilizing the Cosmic Origins Spectrograph (COS) aboard the Hubble Space Telescope (HST) with the G140L grism. The UV spectra of Mrk 478 were acquired on the 5 December 1996, utilizing the HST’s Faint Object Spectrograph (FOS) and employing the G130H and G190H grisms. For Fairall 9, UV spectra were collected on the 22 January 1993, utilizing the HST’s FOS with the G190H and G270H grisms, and subsequently on the 18 July 2012, employing the HST’s COS with the G130M and G160M grisms.

- For NGC (New General Catalog) 1275, the data were sourced from Ref. [27]. Optical spectra encompassed various observations spanning the period from 1983 to 2017. Additionally, UV spectra were acquired from the HST MAST (Mikulski Archive of Space Telescope), with FOS observations in 1993 and COS observations in 2011.
- For PHL (Palomar Haro Luyten) 1092, data were drawn from [28]. Optical spectra were collected using the Goodman spectrograph at the 4.1-meter telescope of the Southern Observatory for Astrophysical Research (SOAR) on the night of 12 December 2014. The UV spectra were obtained using the HST's Space Telescope Imaging Spectrograph (STIS) on the night of 20 August 2003.

In addition, we considered:

- composite spectra for radio-loud (RL) and radio-quiet (RQ) Pop. B sources. The data on which the composites were based were described in previous papers ([21] and references therein);
- median results for two samples of xA sources at intermediate redshift ( $z \approx 2$ ) [22,29] lacking the rest-frame optical spectrum.

### 3. Methodology and Data Analysis

#### 3.1. Multicomponent Analysis

A crucial technique in quasar studies is multicomponent analysis, which involves dissecting complex emission line profiles into distinct components. This approach allows us to uncover details about different regions of emission, potentially revealing information about kinematics, velocities, and structures. Line ratios, such as those involving  $\text{CIV}\lambda 1549$ ,  $\text{HeII}\lambda 1640$ ,  $\text{AlIII}\lambda 1860$ , and  $\text{SiIV}+\text{OIV}\lambda 1402$ , are used as diagnostic tools to infer physical conditions, such as ionization and metallicity, within the quasar environments. In the spectra of quasars, both optical low-ionization and UV high-ionization lines (LILs and HILs, respectively) are observed, and they provide valuable insights into the physical conditions and structure of the quasar BLR. These lines are emitted, at least in part, in distinct regions with different characteristics [30,31].

We distinguish a broad component (BC) that is broadened by the Doppler effect due to the rapid motion of the gas in the BLR in a velocity field dominated by Keplerian motions [32,33]. Lines meeting this condition are also referred to as “virialized broad emission lines”. The LILs like  $\text{H}\beta$  and  $\text{MgII}\lambda 2800$  are typically emitted in the virialized BLR, which may be characterized by high densities and column densities, but with relatively low ionization (ionization parameter  $\sim 10^{-2}$ ). The HILs like  $\text{CIV}\lambda 1549$ ,  $\text{HeII}\lambda 1640$  and  $\text{NV}\lambda 1240$  are also emitted in the virialized BLR. However, these lines mostly trace the regions of the BLR that are exposed to the most intense and energetic radiation from the accretion disk [30,31]. The HILs are often broader than LILs due to higher velocities in the corresponding part of the BLR, and show prominent blueshifts [34,35].

In brief, we subdivide all lines into three main components that can account for the diversity of line profiles, along the quasar MS, resulting from the balance between gravitation and radiation forces [36].

##### 3.1.1. Population A

- Broad Component (BC): represented by a Lorentzian function, symmetric and unshifted or slightly redshifted [4,37].
- Blueshifted Component (BLUE): defined as the excess of emission on the blue side of the BC. The shape can be irregular, but the profiles resemble “triangular” or “trapezoidal shapes” [38,39] that are usually well-modeled by asymmetric Gaussian [38,40]. The blueshifted component can be prominent at high Eddington ratios and high luminosity, dominating the HIL emission [41–43]. The BLUE is increasing in prominence in the HILs along the quasar main sequence and reaches its maximum at STs A3–A4, where  $R_{\text{FeII}} = \text{FeII}\lambda 4570 / \text{H}\beta$  is also at a maximum.

The two components most probably represent coexisting regions [44], albeit in quite different physical and dynamical conditions. While the BC is associated with a dense, low ionization region, capable of emitting mainly (but not exclusively) LILs and maintaining a virialized velocity field (for which a large column density is needed [45]), the outflowing gas should be of higher ionization. The assumption that BLUE and BC refer to regions with the same metallicity has been questioned by models of the AGN involving nuclear star formation [46], and for the sake of the current investigation, we consider independent metallicity estimates from BLUE and BC.

### 3.1.2. Population B

- BC: represented by a Gaussian function, symmetric and unshifted or slightly redshifted [4].
- Very Broad Component (VBC): represented by a Gaussian function, redshifted by about 2000 km/s [4,47]. Given the virial velocity field of the emitting regions, this component represents the innermost emission of the BLR. Several studies have described the Pop. B Balmer profiles in terms of a BLR and a ‘very broad’ line region (VBLR) [48,49]. It is unclear whether the emitting gas might be so highly ionized to be optically thin to the Lyman continuum [50]. The origin of the redshift is the subject of current debate, and two main alternatives have been proposed: gravitational redshift [51–56], and infall [57]. The data support the gravitational redshift hypothesis for  $\log M_{\text{BH}} \gtrsim 8.7 [M_{\odot}]$ , while lower black hole masses,  $M_{\text{BH}}$ , require noticeably low ratio of the object bolometric luminosity to the Eddington luminosity,  $L/L_{\text{Edd}}$ , for the profiles to show a significant gravitational effect [58].
- BLUE: defined as the excess of emission on the blue side of the sum of BC and VBC profile. The blueshifted component is usually not prominent at low Eddington ratios but can however affect the centroid and asymmetry index of both HILs and LILs. Due to its weakness, BLUE is always modeled by a shifted (symmetric) Gaussian.

Figure 1 summarizes the interpretation of the line profiles of CIV and H $\beta$  assumed as prototypical HIL and LIL, respectively, for Pop. B, Pop. A, and xA. Since BLUE is barely resolved in Pop. B, no estimates of the metallicity  $Z$  are considered here. For xA objects, an estimate has been carried out for BC and BLUE, while for Pop. B sources, for the BC and VBC. In the latter case, one expects that the metallicity is the same, but the physical conditions would reflect a gradient in ionization (lower ionization for the BC and higher for the VBC), and hence be different on average.

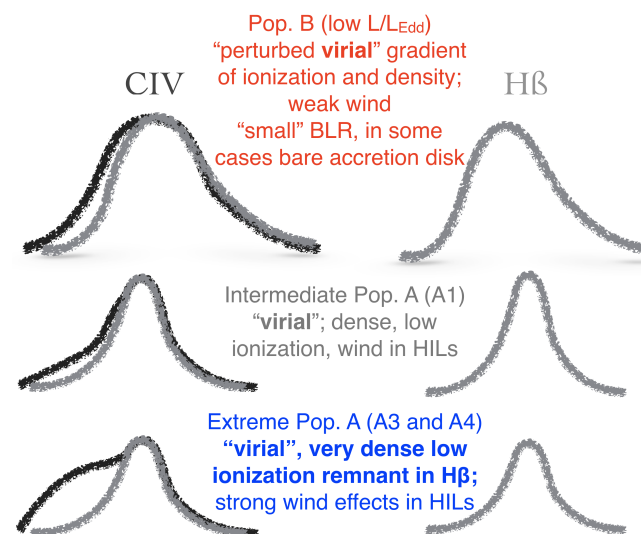


**Figure 1.** Interpretation of the line profiles of low-ionization and high-ionization lines (LILs and HILs, respectively) along the MS, for isolating major spectroscopically resolved components. ‘Pop.’ stands for ‘Population’. See text for details.

### 3.2. Emission Line Ratios

- Z indicator  $CIV/SiIV+OIV\lambda 1402$  has been extensively applied as metallicity indicator (e.g., [13,16]). In photoionization equilibrium, the classical argument derived for HII regions that the electron temperature decreases with increasing metallicity [59] works for the BLR as well. The intensity of the CIV line actually decreases as the metal abundance increases. However, the reason why the ratio CIV/SiIV is a metallicity indicator resides in the “competition” of He<sup>+</sup> ions that have roughly the same creation potential of C<sup>++</sup>. As a result, the Strömgren sphere of C<sup>+3</sup> decreases much more strongly with increasing Z than for Si<sup>+3</sup>: the ionization potential of Si<sup>+2</sup> is 2.46 Ryd, so the relatively unabsorbed continuum between 2.5 Ryd and 3.5 Ryd is available to maintain a proportionality with its abundance [60]. This effect dominates over the lower electron temperature that affects the collisional excitation rates of both SiIV and CIV, expected to be higher for SiIV.
- Z indicators CIV/HeII $\lambda 1640$  and SiIV/HeII $\lambda 1640$ : when considering indicators like CIV/HeII $\lambda 1640$  and SiIV/HeII $\lambda 1640$ , those indicators should show sensitivity to the abundance of carbon and silicon, assuming that the ratio of helium relative to hydrogen remains constant. However, the dependence of CIV/HeII $\lambda 1640$  on Z is not monotonic: it increases for sub-solar metallicities and then declines steadily up to  $200Z_{\odot}$ , for specific conditions with the ionization parameter,  $\log U \approx 0$ , and the hydrogen density,  $\log n_H \approx 9 \text{ cm}^{-3}$  [22]. For lower U values, the behavior is monotonic [29]. This stresses a need for multiple intensity ratios that depend on Z and U.
- Z indicators involving NV, NV/CIV and NV/HeII $\lambda 1640$  have also been extensively employed in previous studies [12,13,16,61,62]. The strength of the NV line was found to be unexpectedly high in a photoionization scenario, possibly due to a selective enhancement of nitrogen (e.g., [63,64]), resulting from secondary production of nitrogen by massive and intermediate-mass stars, and yielding a nitrogen-to-hydrogen abundance ratio  $[N/H] \propto Z^2$  [15,65,66]. This process can be particularly significant in cases of abnormal star formation and evolution processes that are expected to occur within active nuclei. Contamination by narrow and semi-broad absorption features is often significant, and even with precise modeling of high-ionization lines, it may be challenging to reconstruct the unabsorbed profile of the red wing of Ly $\alpha$ . In this analysis, we refrain from using ratios involving NV because they are not consistently measurable.
- Density indicators. The ratios AlIII/SiIII] and SiIII]/CIII] are responsive to density since they involve intercombination lines with well-defined critical densities ( $n_c \sim 10^{10} \text{ cm}^{-3}$  for CIII] [62] and  $n_c \sim 10^{11} \text{ cm}^{-3}$  for SiIII]).
- Ionization parameter SiIII]/SiIV, SiII $\lambda 1814$ /SiIII], and SiII $\lambda 1814$ /SiIV are influenced by the ionization parameter and remain insensitive to changes in Z since the lines are from different ionic states of the same element. Also, the ratio CIII]/CIV is sensitive to the ionization parameter but entails a strong dependence on the  $n_H$  as well. The ratio CIV/H $\beta$  is also a indicative diagnostic, although it is also dependent on Z but often made unreliable by the intrinsic variations of the quasar and by poor photometric accuracy if observations are not synoptic and dedicated.
- Mixed diagnostics: FeII/H $\beta$ . The ratio  $R_{FeII}$  deserves particular attention. As with any other metal to hydrogen ratio, it entails an expected dependence on iron abundance and hence on metallicity. Nonetheless,  $R_{FeII}$  is dependent on density, ionization parameter and column density,  $N_c$ , of the line emitting gas, in the sense that large  $R_{FeII}$  ( $\gtrsim 1$ ) seem possible only for relatively high  $n_H$  ( $\gtrsim 10^{11} \text{ cm}^{-3}$ ), low ionization and large  $N_c$  ( $\gtrsim 10^{23} \text{ cm}^{-2}$ ) [7,67,68].

In what follows, we use the same ratios as much as possible for the three-line components. However, the BLUEs are often too weak to be detectable in several LIL profiles. In this case, we consider upper or lower limits as appropriate. Table 1 provides an overview

of the measured intensity ratios applied to the metallicity estimates of several of the targets here.

**Table 1.** Diagnostic intensity ratios.

Component	SiIV+OIV/ CIV	SiIV+OIV/ He II <sub>UV</sub>	CIV/ He II <sub>UV</sub>	CIV/ CIII]	CIV/ Hβ	AlIII/ CIV	AlIII/ He II <sub>UV</sub>	AlIII/ SiIII]	SiIII/ CIII]	R <sub>FeII</sub>	HeII <sub>opt</sub> Hβ
BLUE [A]	○	○	○	—	>	<	<	—	—	<	—
BC	○	○	○	○	○	○	○	○	○	○	<
VBC [B]	○	○	○	○	○	○	—	<	<	○	○

○ measured ratio with associated uncertainty. < and >: upper and lower limit to intensity ratio, respectively. —: not available. HeII<sub>UV</sub> and HeII<sub>opt</sub> are HeIIλ1640 and HeIIλ4686, respectively. Blue circles identify the ratios actually used for the new sources presented in this paper; the use of the CIV/Hβ ratio has been considered only for Fairall 9, due to the non-contemporaneity of the rest-frame optical and UV data. Unavailable ratios involve two undetectable components. See text for details.

### 3.3. Photoionization Simulations

Understanding the physical conditions within quasar environments involves estimating parameters such as the metallicity ( $Z$ ), density ( $n_H$ ), and ionization state (ionization parameter,  $U$ ). The three fundamental parameters can be estimated by comparing observed line ratios with model predictions obtained through computational models, such as CLOUDY, which simulate the interactions between radiation and gas in the environments of the broad line region [69]. Input parameters for photoionization computations are the photoionizing continuum spectral energy distribution (SED), the ionization parameter (or an alternative, luminosity, and distance of the emitting region), gas hydrogen density, chemical composition, and a micro-turbulence parameter. There is evidence of trends for all of these parameters along the quasar main sequence, and in the case of Pop. B, there is evidence of a radial stratification of the properties within the BLR [70,71] that is heuristically modeled separating a BC and VBC (BLR and VBLR).

The arrays of simulations were therefore organized as follows: five different SEDs, one for each of the following cases: Pop. B RL, Pop. B RQ, with a dedicated SED for NGC 1275, an SED for Pop. A sources [72] and one for extreme Pop. A (high Eddington ratio of Ref. [73]). Metallicity was assumed to scale as the solar  $Z_\odot$ , with twelve values spanning  $0.01 Z_\odot$  to  $1000 Z_\odot$  for Pop. A and fourteen values between  $0.001 Z_\odot$  and  $20 Z_\odot$  for Pop. B. The micro-turbulence parameter was set to 0 km/s. This is relatively insignificant for resonance UV lines [22], but is expected to lead to an under-prediction of FeII emission [22,74,75]. For each metallicity value, we considered an array of simulations covering the  $n_H$ - $U$  plane in the range  $7 \leq \log n_H \leq 14 \text{ cm}^{-3}$ ,  $-4.5 \leq \log U \leq 1$  for Pop. A (667 simulations), and  $7 \leq \log n_H \leq 13 \text{ cm}^{-3}$ ,  $-3 \leq \log U \leq 1$  for Pop. B (425 simulations). For each source or composite spectra, the set of 8–9 diagnostic ratios were compared with a set of about 8000 and 6000 simulations covering the parameter space  $n_H$ ,  $U$ , and  $Z$ , for Populations A and B, respectively. The computations were carried out independently for the three components identified in the emission lines, as they are thought to represent distinct regions in different physical conditions. The solution for the single zone model (i.e., a single point in the 3D space of  $n_H$ ,  $U$ , and  $Z$ ) was identified by the  $\chi^2$ -statistics minimum computed from the difference between the observed line ratios and the predicted line ratios over the entire 3D space (see, e.g., [22,29]).

The errors on measured line ratios were estimated assuming that the continuum placement was the dominant source of uncertainties and setting extreme continua as ‘cont ± rms’ where ‘const’ is the best-fit continuum and ‘rms’ (root mean square) is the noise measured over the continuum itself and propagated according to the “triangular distribution” [76]. Limits at  $1\sigma$  (standard deviation) and 90% confidence were set by computing the ratio  $F = \chi^2 / \chi^2_{\min}$  between  $\chi^2$  of different models for  $(n_{\text{ratios}} - 3)$  degrees of freedom.

There are several caveats in the method, related to both the quality of the data and the model assumption: (1) the non-simultaneity of the observations in the optical and UV. Often, optical and UV observations are separated by years in the rest frame of a quasar. In addition, the photometric inter-calibration between the optical and the UV data is problematic: while space-based observations are precise within a few percent, the optical data are affected by uncontrolled light loss. As a result, the ratio  $C_{IV}/H\beta$  was measured but ultimately removed from the computations in the new sources analyzed in the present paper (Mrk 335, Mrk 478, PHL 1092) except for Fairall 9. In this case, simulations both with and without the ratio  $C_{IV}/H\beta$  were run and gave consistent results. (2) A major assumption is that metallicity scales as solar. Albeit this is a time-honored assumption [77,78], it is not a reasonable one because major differences are expected for a disk star in a late-type spiral galaxy and the nuclear region of an active galaxy (see [79] and references therein). Actually, recent studies discussed the evidence of pollution by supernova ejecta [29,80]. (3) Photoionization computations are carried out under the assumption of single-zone emission. While this assumption seems to be a suitable one for  $\chi A$ , where density and ionization tend toward the limiting values [7], this might not be the case for Pop. B sources.

#### 4. Case Studies

The basic properties of the cases considered in this paper are reported in Table 2, and include the E1 optical parameter FWHM  $H\beta$  and  $R_{FeII}$ , as well as the accretion parameters (luminosity,  $M_{BH}$ , and Eddington ratio). The last columns provide the radio loudness parameter and some notes that list bibliographical sources of information or notable, recent studies related to the specific object.

- Composite RL ST B1. A RL composite spectrum was obtained from 20 RL sources, with redshift range of about 0.25–0.65, absolute magnitudes between  $-23.5$  and  $-26.5$  and the signal-to-noise ratio,  $S/N \approx 130$  and  $\approx 55$  for the visual and UV ranges. The  $Z$  estimates are used as given in Ref. [21] since the method of analysis and measurement is basically the same.
- NGC 1275. NGC 1275 (Perseus A) is an elliptical galaxy, and the brightest cluster galaxy of the Perseus Cluster, one of the most massive galaxy clusters in the nearby Universe. NGC 1275 is associated with a cooling flow phenomenon, where gas in the cluster's intracluster medium is thought to cool and sink towards the central regions of the galaxy [81,82], potentially fueling its modest AGN activity. The photoionizing continuum, which is crucial for understanding the ionization state of the gas in NGC 1275, was defined ad hoc by observational constraints on the SED (see [27] for details). The estimated photoionizing continuum had a spectral index  $\alpha_\nu = 0.5$  in the far-UV range  $500 \text{ \AA}$  to  $800 \text{ \AA}$  and a spectral break at  $800 \text{ \AA}$ . Beyond this spectral break, the spectral index  $\alpha_\nu = 2$  down to the soft X-ray band at  $0.5 \text{ keV}$ , with  $\alpha_\nu = 1.0$  in the harder X-ray band. In summary, the SED of the far-UV shown in Ref. [27] indicates a broad line Seyfert-like AGN with a soft ionizing continuum, a weak hard ionizing continuum, and no Compton reflection hump. The big blue bump associated with thermal emission from optically thick, geometrically thin accretion [83] is weaker than the ones of the SED templates appropriate for Pop. B quasars; see Figure 5 in Ref. [27]. The  $L/L_{Edd}$  is too low and, interestingly, the BLR is correspondingly weak, to the point that a careful, dedicated analysis was needed to disentangle the broad line profiles from the considerably stronger narrow line emission.
- Composite RQ ST B1. A composite spectrum was constructed for a group of 16 RQ sources, all falling within the spectral bin B1, within the redshift range of redshift range approximately 0.002–0.5. These sources span an absolute magnitude range  $-21$  to  $-27$ , which corresponds to a bolometric luminosity range  $\log L \approx 45\text{--}47 \text{ erg/s}$ . To achieve comprehensive UV coverage from  $1000 \text{ \AA}$  to around  $6000 \text{ \AA}$  (including the spectral region from  $Ly\alpha$  to  $H\beta$ ), which is typically demanding and necessitates space-based observations, the UV data were obtained from HST/FOS observations as discussed in Ref. [84]. Additionally, the optical spectra were sourced from Ref. [26].

The composite spectrum has quite a high S/N, of approximately 90. The metallicities for this composite and their corresponding uncertainties were adopted from Ref. [21].

- Fairall 9 ST B1. Empirical parameters derived from the MS analysis indicate Fairall 9's spectral type as B1, a category well-populated among quasars along the MS. This classification consistently aligns with a low  $L/L_{\text{Edd}}$  ratio. Notably, Fairall 9 exhibits radio quietness, as it eluded detection in the Sydney University Molonglo Sky Survey [85] with a detection limit of 6 mJy, implying a radio-to-optical specific flux ratio of not exceeding 1.5. We use the Kellerman ratio,  $\log R_K \approx -0.04$  [86].  
The most recent assessment of the black hole mass includes estimates using the reverberation mapping technique that have converged on the values spanning  $(1.5 \text{ to } 2.5) \times 10^8 M_{\odot}$  [87,88], contingent on the adopted virial factor, as well as a spectropolarimetric-derived  $M_{\text{BH}}$  that allowed for a virial factor estimate, yields  $(1.5 \pm 0.5) \times 10^8 M_{\odot}$ . A conventional estimate of Fairall 9's bolometric luminosity stands at  $\log L_{\text{bol}} \approx 45.3 \text{ erg/s}$ , with an Eddington ratio of  $\log L/L_{\text{Edd}} \approx -2.0$ , placing it toward the lower end within the distribution of Pop. B sources. The SED also conforms to the characteristics of Pop. B objects, devoid of a prominent big-blue bump. More details are given in a recent paper [89].
- Mrk 335 ST A1. Mrk 335 is a Pop. A Seyfert 1. It is located in the nearby Universe with a redshift of 0.0256. This AGN exhibits characteristics typical of an RQ A1 AGN, with lower-than-average FeII emissions, positioning it in the lower-left corner of the MS. Emission lines in the UV and optical ranges exhibit little to no blueshifts in their profiles. The only exception to this typical behavior is the slope of its optical continuum, which is likely due to galactic extinction.
- Mrk 478 ST A2. Mrk 478 is a Pop. A Seyfert 1, borderline ST A3 from the measurements of the present analysis. It is located at a redshift of 0.077. Although classified as A2, it exhibits characteristics that suggest it may be an extreme accretor. Table 2 shows that it has the Eddington ratio about 1. Additionally, it displays a strong FeII emission and a pronounced outflowing component in its emission line profiles. Hence, it could be argued that Mrk 478 could be classified as an A3-type object.
- PHL 1092 ST A4. PHL 1092 is a Pop. A Seyfert 1, spectral type A4, located at a redshift of 0.3965. Its spectrum is characterized by strong UV emissions, with a notably sloped X-ray SED. PHL 1092 is considered an extremely accreting quasar, as it exhibits prime characteristics of one, including a strong outflowing component in its emission line profiles, particularly noticeable in  $\text{CIV}\lambda 1549$  and  $\text{SiIV+OIV}\lambda 1402$ , which casts a shadow on the virialized component. In the optical range, the  $\text{H}\beta$  emission is overshadowed by the FeII emission, mirroring the FeII profile of I Zw 1, itself considered an extreme accretor.
- Extreme Population A STs (A3, A4). The intermediate-redshift xA sample of Refs. [22,29] allowed for  $Z$  estimates from the UV spectral lines. The sample lacks the optical data providing the essential information from the  $\text{H}\beta$  spectral range, and the line width reported in Table 2 is the one of AlIII. The sources were selected based on UV criteria that were found equivalent to the criterion  $R_{\text{FeII}} \gtrsim 1$  for the identification of xA sources, at least at a high degree of confidence [90]. Their luminosity is significantly higher than the luminosity of the other sources considered in this paper, although the Eddington ratio is consistent with the ones of Mrk 478 and PHL 1092 of about  $\mathcal{O}(1)$ .

**Table 2.** Object properties.

Object	ST <sup>(a)</sup>	$z$ <sup>(b)</sup>	FWHM(H $\beta$ ) <sup>(c)</sup> [km s <sup>-1</sup> ]	$R_{\text{FeII}}$ <sup>(d)</sup>	$L_{\text{bol}}$ <sup>(e)</sup> [erg s <sup>-1</sup> ]	$M_{\text{BH}}$ <sup>(f)</sup> [ $M_{\odot}$ ]	$L/L_{\text{Edd}}$ <sup>(g)</sup>	$R_{\text{K}}$ <sup>(h)</sup>	Comment
Composite RL	B1	$\approx 0.25\text{--}0.65$	7690	0.17	$8 \times 10^{44} \text{--} 8 \times 10^{45}$	$10^8\text{--}10^9$	0.01–0.1	$\gtrsim 80$	[21]
NGC 1275	B1	0.017	4770	n.d. <sup>(i)</sup> , $\lesssim 0.2$	$1.2 \times 10^{43}$	$8 \times 10^8$	$\lesssim 10^{-4}$	1744	$L/L_{\text{Edd}}$ , $M_{\text{BH}}$ , $L_{\text{S}}$ : [27]
Composite RQ	B1	$\approx 0.002\text{--}0.5$	5530	0.34	$8 \times 10^{43} \text{--} 2 \times 10^{46}$	$4 \times 10^8\text{--}10^9$	0.01–0.04	$\lesssim 10$	[21]
Fairall 9	B1	0.04609	4550	0.43	$2 \times 10^{45}$	$1.5 \times 10^8$	0.01	0.92	$R_{\text{K}}$ : [86], $M_{\text{BH}}$ : [89]
Mrk 335	A1	0.0256	2175	0.34	$6.9 \times 10^{44}$	$3.45 \times 10^7$	0.13	0.36	
Mrk 478	A2/A3	0.077	1322	1.04	$4.4 \times 10^{45}$	$2.90 \times 10^7$	1.02	0.85	[91–93] Radio- detected but RQ [28,94]
PHL 1092	A4	0.3965	2494	1.76	$1.4 \times 10^{46}$	$2.21 \times 10^8$	0.42	0.78	
Composite	xA	2.1–2.5	3200 <sup>(j)</sup>	... <sup>(j)</sup>	$4 \times 10^{46} \text{--} 4 \times 10^{47}$	$10^9 \text{--} 10^{10}$	0.7–3	$\lesssim 80$	$<L/L_{\text{Edd}}>$ $\approx 1$ ; [22,29]

<sup>(a)</sup> Spectral type of the object. <sup>(b)</sup> Redshift. <sup>(c)</sup> Full width at half maximum of H $\beta$ . <sup>(d)</sup> FeII prominence parameter, defined as the intensity ratio  $R_{\text{FeII}} = \text{FeII}\lambda 4570/\text{H}\beta$ . <sup>(e)</sup> Bolometric luminosity obtained by integrating the specific flux obtained from the NED (NASA/IPAC Extragalactic Database) over all frequencies. <sup>(f)</sup> Mass of the supermassive black hole of AGNs calculated using the scaling relation from Ref. [95]. <sup>(g)</sup> Ratio between the bolometric luminosity of the object and the Eddington luminosity:  $L/L_{\text{Edd}} = L_{\text{bol}}/[1.5 \times 10^{38} (M_{\text{BH}}/M_{\odot})]$ . <sup>(h)</sup> Kellerman ratio obtained from  $f_{\text{radio}}/f_{\text{B}}$  [96], where  $f_{\text{radio}}$  is the specific flux at the wavelength of 6 cm (5 GHz) and  $f_{\text{B}}$  is the specific flux at 4400 Å (680 THz) in the B band. <sup>(i)</sup> Not detected, only a broad upper limit is estimated. <sup>(j)</sup> H $\beta$  spectral range not covered:  $R_{\text{FeII}}$  not available. The FWHM refers to the best proximate of H $\beta$  in the UV, the AlIII doublet. See text for more details.

## 5. Results

### 5.1. Line Profile Analysis

The results of the line profile analysis are shown, as an example, for Fairall 9 (Figure 2). All the lines fit with the three components introduced in Section 3.1. HeII $\lambda$ 1640 and CIV are explained assuming that the components are present with consistent shifts and widths but changing their relative intensity ratios. This accounts for the flat HeII $\lambda$ 1640 profile that lacks the prominent BC observed for CIV, in turn implying CIV/HeII $\lambda$ 1640  $\gg 1$  for the BC. The VBC CIV/HeII $\lambda$ 1640 is essentially lower. A similar effect is visible for H $\beta$  and HeII $\lambda$ 4686 in Figure 2, top right). This has implications on the physical conditions derived for the VBLR and BLR, in turn motivating the model with two separate components, as discussed in several studies [97–99]. Another key implication is that the VBC of HeII $\lambda$ 4686 and HeII $\lambda$ 1640 is considerably better defined than the BC, allowing for a more reliable estimate of the VBC ratios involving these lines.

Similar line profile decomposition has been carried out for quasar emission lines over a broad range of redshift [41,100,101]. The heuristic technique applied in this and some previous papers allows to consistently fit all quasars emission lines with only three components, and is equivalent to measuring profile intensity ratios [29,102], with the advantage that the absorptions that are frequently found in high-redshift quasar spectra can be compensated. Intensity ratios for the three components are found consistent with those from profile ratios [29].

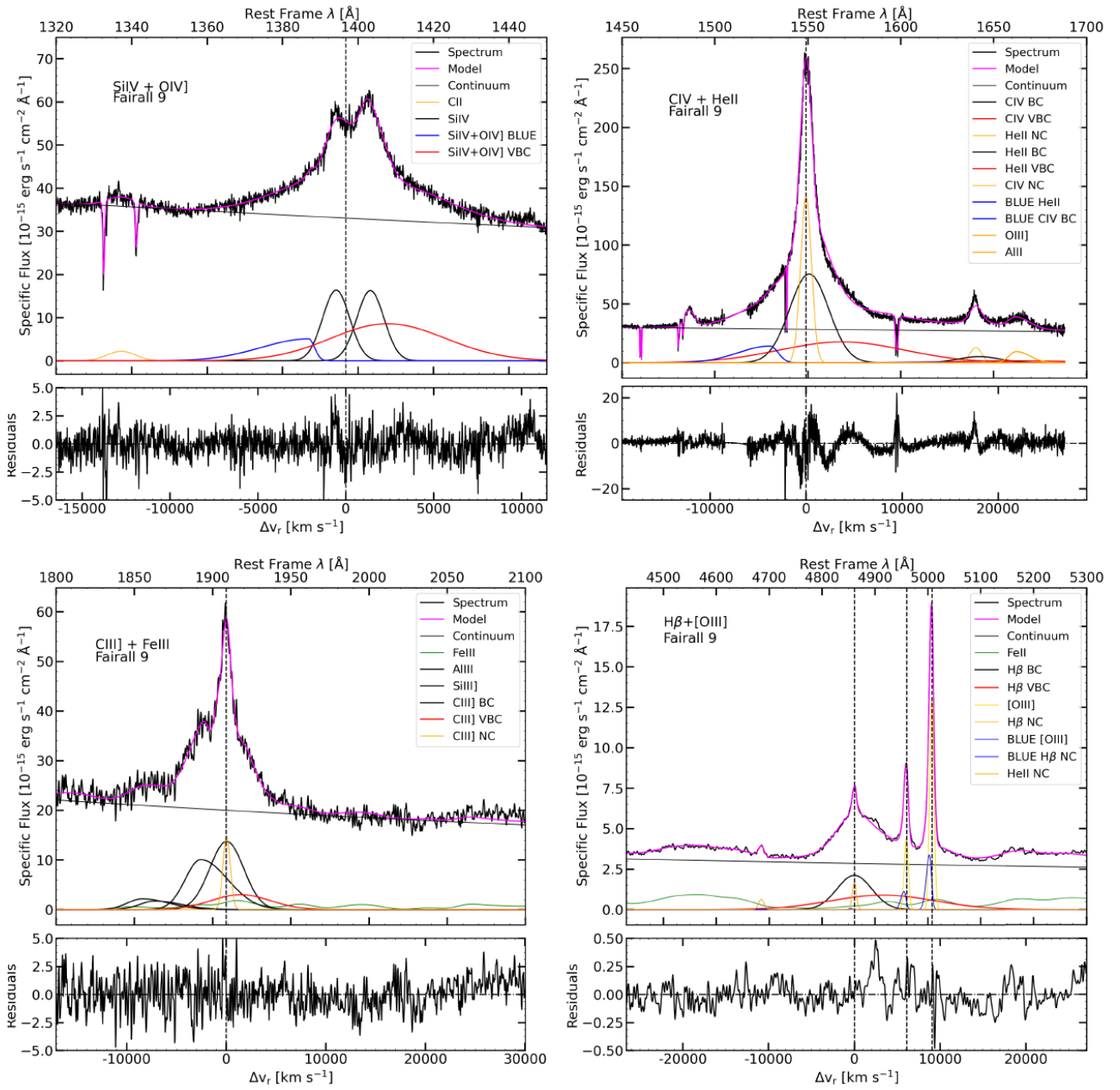


**Figure 2.** Fits of the emission line spectrum of Fairall 9, the prototypical Population B source: 1400 Å (top left), CIV + HeII $\lambda$ 1640 (top right), 1900 Å (bottom left), H $\beta$  + FeII (bottom right) blends. The emission line profiles of H $\beta$  and the 1900 Å blend are accounted for by two components, BC (black lines) and VBC (red). The HILs in the rest-frame UV show an excess with respect to the BC plus VBC extending on the blue side of the emission line, modeled with a skew Gaussian [103] and ascribed to emission from a spectroscopically resolved outflow that adds up to the virialized components. The magenta lines trace the full empirical model of the emission line profiles. The box under each spectra plot shows the difference between the observed spectrum and the computed one. See text for more details.

### 5.2. Estimation of Metallicity for the Virialized Emitting Region

Four of the case studies are new results on individual objects, and the metallicity values and the associated uncertainties at  $1\sigma$  confidence level are reported in Table 3, along with estimates from earlier published studies. Figures 3 and 4 show the interval of

confidence at  $1\sigma$  level for the new cases in the planes of  $Z$  versus ionization parameter  $U$  and density  $n_H$ .

**Table 3.** Metallicity estimates along the quasar MS. See text for details.

Identification	Component	$\log(Z/Z_\odot)$	$1\sigma$ range	Comment
Composite RL B1	BC	−1.70	−2.00 — −1.00	[21]
NGC 1275	BC	−0.30	−0.30 — 0.00	[27]
Composite RQ B1	BC	0.30	−0.70 — 1.00	[21]
Composite RQ B1	VBC	0.70	0.70 — 0.70	[21]
Fairall 9	BC	0.30	−1.30 — 1.00	This study; $C_{IV}/H\beta$ excluded
Fairall 9	VBC	0.00	0.00 — 0.30	This study; $C_{IV}/H\beta$ excluded
Fairall 9	BC	0.00	−1.00 — 0.70	This study
Fairall 9	VBC	0.30	0.30 — 0.30	This study
Mrk 335	BC	0.00	−1.00 — 0.00	This study
Mrk 478	BC	1.30	1.00 — 1.30	This study
PHL 1092	BC	1.70	1.30 — 2.30	This study
Composite $x_A z \approx 2$	BC	1.70	1.30 — 2.00	[22,29]

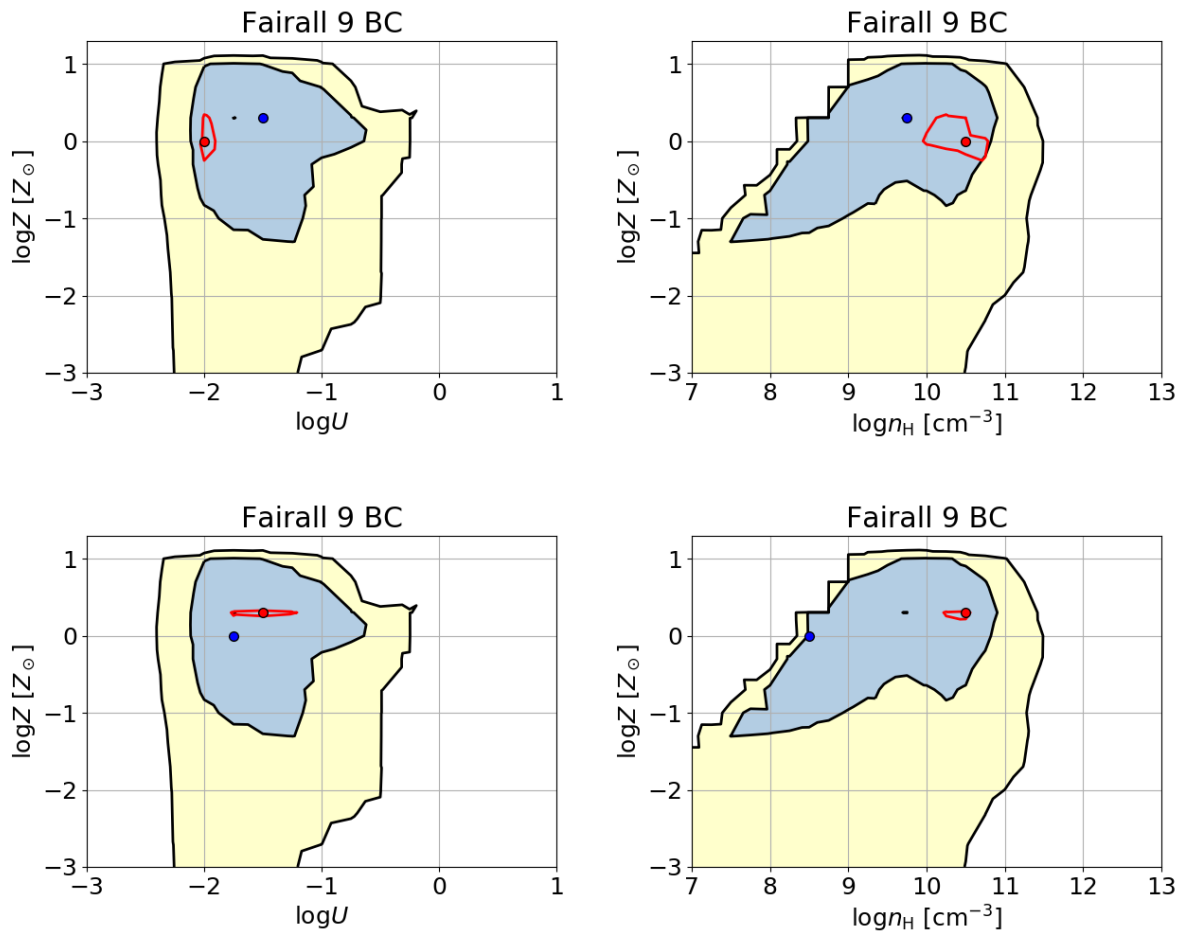


**Figure 3.** Projections of the 3D parameter space ( $U, n_H, Z$ ) onto the ( $U, Z$ ) (left) and ( $n_H, Z$ ) planes (right), for the prototypical Population B source Fairall 9 for  $\chi^2$  computed with (top) and without (bottom)  $C_{IV}/H\beta$  ratio. The blue and red spots identify the model yielding  $\chi^2$  minimum for the BC and VBC, respectively. The color areas represent the isophotal areas of  $1\sigma$  (pale blue) and 90% confidence level (yellow). The red boundary line shows the  $1\sigma$  level for the VBC. See text for details.

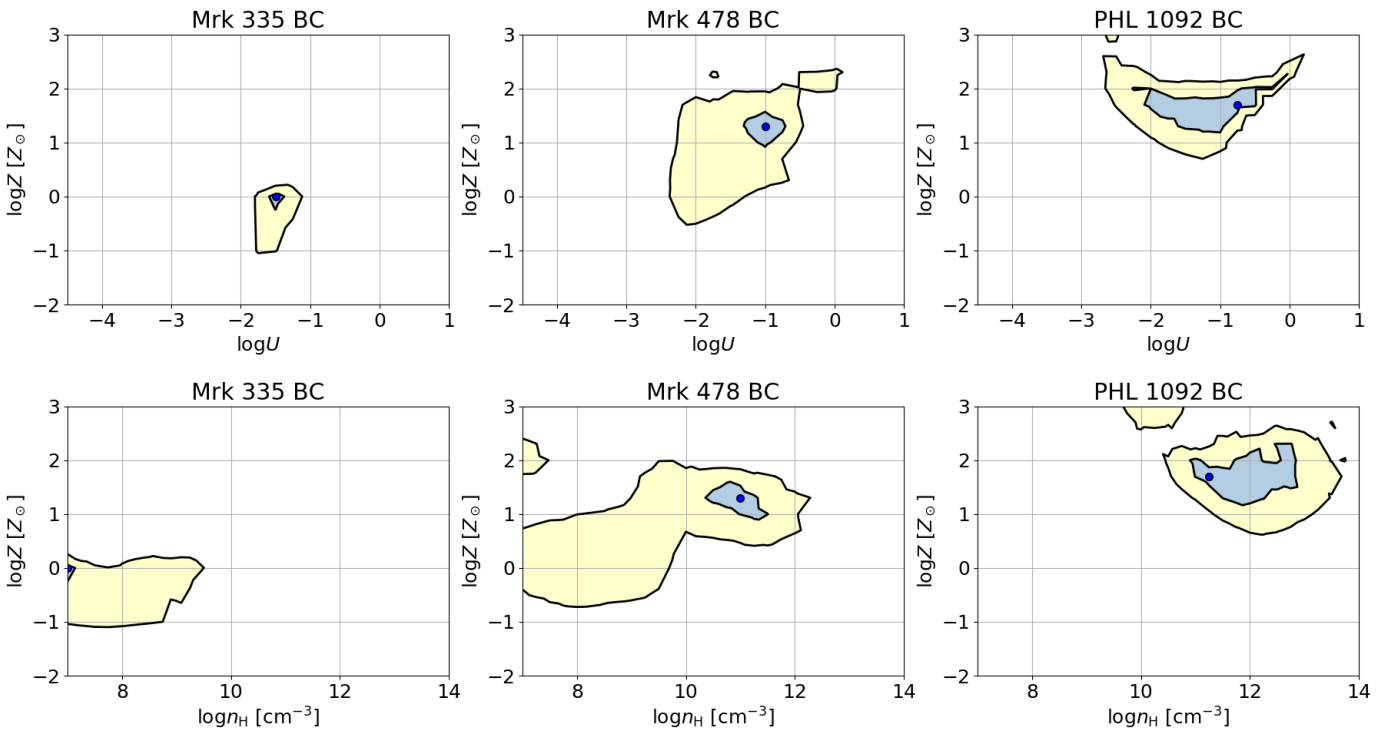


**Figure 4.** Projections of the 3D parameter space ( $U$ ,  $n_H$ ,  $Z$ ) onto the ( $U$ ,  $Z$ ) (top) and ( $n_H$ ,  $Z$ ) planes (bottom), for the Population A sources Mrk 335 (left), Mrk 478 (middle), and PHL 1092 (right). The colors of the isophotal areas are of the same meaning as in Figure 3.

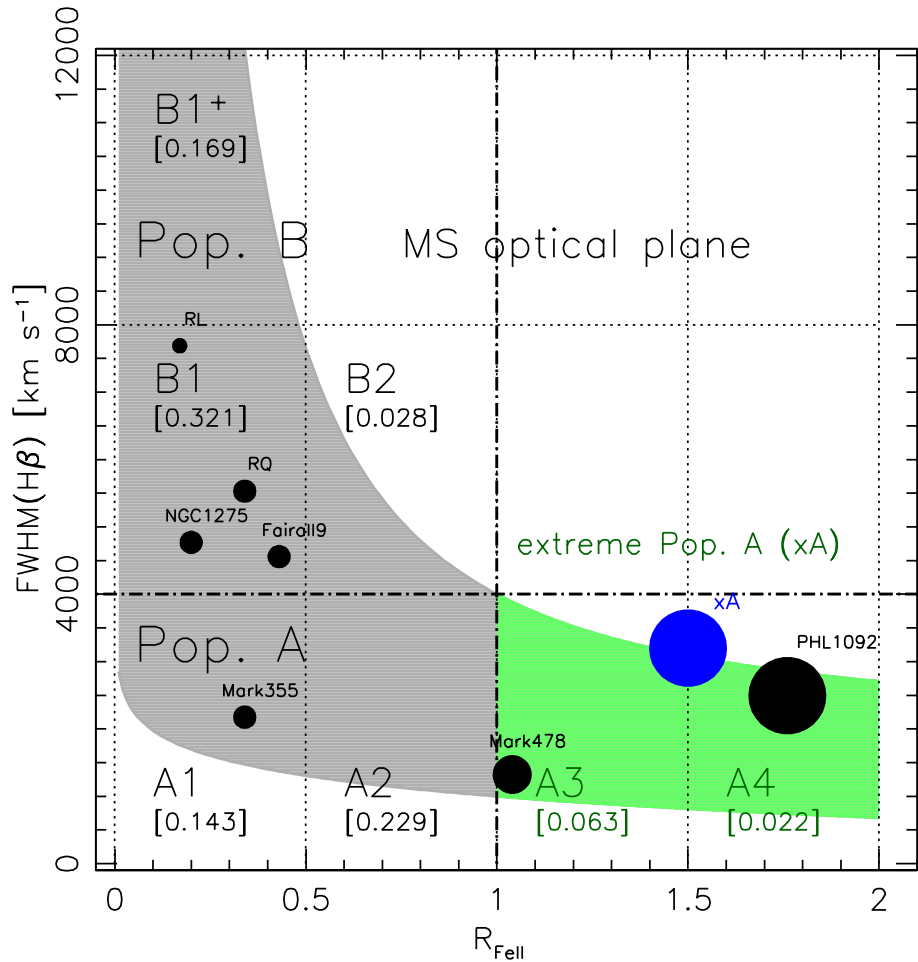
The case of Fairall 9 includes the best  $Z$  derived for the VBLR. The  $\chi^2$  is of quite low values even if the number of degrees of freedom is small enough, which allows for a much more restricted range in the parameter space than for the case of the BLR ratios. For the case of Fairall 9, the parameters are rather loosely constrained, although the agreement between the  $\chi^2$ -minimum derived for the BC and the one of the VBC, reinforces a metallicity estimate  $Z \approx (1 - 2)Z_\odot$ , as the two regions are expected to have the same  $Z$ . In the Fairall 9 case, the consideration of the ratio  $C_{IV}/H\beta$  (a key parameter connected, in addition to  $Z$ , also to  $U$ ), confirms the estimate of  $Z \approx (1 - 2)Z_\odot$  for both the BLR and VBLR.

Figure 4 shows the planes of  $Z$  versus ionization parameter  $U$  and density  $n_H$  ordered along the sequence of increasing  $R_{FeII}$  within Pop. A. The  $Z$  values range from  $Z \lesssim 0.1Z_\odot$  to  $50Z_\odot$  for the B1 RL composite to PHL 1092. The  $Z$  value obtained for PHL 1092 confirms the high  $Z \approx 100Z_\odot$  obtained with UV intensity ratios only [22,29].

Figure 5 shows the location of all case studies along the E1 main sequence. The  $Z$  values along the main sequence range from  $0.1Z_\odot$  to about  $100Z_\odot$ , and the trend is one of a monotonic increase along the horizontal sequence of increasing  $R_{FeII}$ , from solar or slightly subsolar, to highly supersolar, with  $Z$  at least a few tens the solar values. STs B1 and A1 consistently show similar values around solar, with weak but nevertheless significant FeII emission.

A vital result is that not all BLRs are made of gas with the same metal content. There is apparently a systematic gradient involving a range of more than a factor of about 100. Disregard the exact values of  $Z$ , especially at the extremes, the trend is substantiated by the trend in the most metal-sensitive ratios,  $(Si_{IV}+O_{IV})\lambda 1402/C_{IV}$ , and  $R_{FeII}$ , and ratios involving AlIII. The range in  $Z$  can be compared with a recent systematic study for intermediate-redshift quasars [20]. The highest values around  $Z \approx 20Z_\odot$  are found for massive black holes ( $\log M_{BH} \approx 9.7 [M_\odot]$ ), and are comparable with the values we obtain at low- $z$  for high Eddington ratio sources.

At intermediate redshift, however, the BLR  $Z$  remains always highly supersolar:  $Z \gtrsim 5Z_{\odot}$ , quite above the most metal-rich galaxies ( $Z \approx 2Z_{\odot}$ ) [78]. Quasars with modest masses ( $\lesssim 10^8 [M_{\odot}]$ ) radiating at low  $L/L_{\text{Edd}}$  are not yet sampled in major surveys at intermediate redshifts. Therefore, the absence of low- $Z$  sources from these surveys does not imply any disagreement.



**Figure 5.** The quasar main sequence (MS) at low redshift mapped on the FWHM( $H\beta$ )– $FeII$  plane. The larger metallicity value, the larger the solid circle size is. Metallicity limits are as follows:  $Z \lesssim 0.1Z_{\odot}$  (smallest size circle),  $0.5Z_{\odot} \lesssim Z \lesssim 2Z_{\odot}$ ,  $Z \approx 10Z_{\odot}$ , and  $Z \approx 50Z_{\odot}$ . The blue circle refers to the intermediate- $z$  sample from Ref. [29]. The numbers in square brackets report the prevalence of each spectral bin in a sample based on the Sloan Digital Sky Survey [104]. The gray and the green areas define the approximate occupation of the MS, with the green area limiting the region with  $R_{FeII} \geq 1$  of  $x_A$  quasars.

### 5.3. Outflows Traced by the Blueshifted Components

Gas outflows appear to be a phenomenon shared by the majority of AGNs (e.g., [105–109]). Emission lines like  $CIV\lambda 1549$  provide valuable information about massive, ionized outflows associated with the accretion disk, and in turn, contribute to understanding the dynamic processes within the BLR and its interplay with the accretion disk.

Selection of the lines most suitable for plasma diagnostics, including the metallicity, is essentially harder for the outflow component than for the virialized one, as the first appears spectroscopically resolved in high- and low-ionization lines only for  $x_A$  or at high luminosity. We used four diagnostic ratios for estimating the physical properties of the blue, outflowing component:  $CIV/HeII\lambda 1640$ ,  $CIV/(OIV]\lambda 1402 + SiIV)$ ,  $CIV/H\beta$  and  $(OIV]\lambda 1402 + SiIV)/HeII\lambda 1640$ , along with constraints from upper limits for the ratios  $AlIII/CIV$ ,  $FeII/H\beta$ . The diagnostic ratios are consistent with the estimates of metallicity

derived for the virialized components, for PHL 1092 ( $Z \approx 50Z_{\odot}$ , with a  $1\sigma$  confidence range 20–50  $Z_{\odot}$ ). Median values of the BLUE components are about  $6Z_{\odot}$  for the xA intermediate- $z$  samples, somewhat lower and obtained only with three diagnostic ratios (H $\beta$  was not measured). Note that this abundance estimate is obtained using ratios involving only  $\alpha$ -elements. Other properties of the outflowing component are less well-constrained because of the limited number of diagnostics. A considerably better precision might be achieved with higher S/N and additional diagnostic ratios. However, it is reasonable to assume that the outflowing gas from the high Eddington ratio sources might have  $Z \approx 10Z_{\odot}$ , a conservative estimate in agreement with other studies ([20] and references therein). If this is the case, the mass outflow rate is  $\dot{M} \sim 10^3 L_{\text{CIV},45} n_{\text{H},9}^{-1}$ , where  $L_{\text{CIV},45}$  is the CIV luminosity in  $10^{45}$  erg/s and  $n_{\text{H},9}$  is the hydrogen density in  $10^9 \text{ cm}^{-3}$  [38]. Solar metallicity implies that 1.46% of the mass of the gas is due to metals. For a modest CIV luminosity of  $10^{44}$  erg/s, the implication is that about  $15 M_{\odot}/\text{yr}$  of metals are returned to the interstellar medium (ISM). Over a high-accretion lifetime of the order of  $10^7$  yr [110,111], the metal mass expected to be returned to the ISM could be of the order of  $10^8 M_{\odot}$ . While this estimate is particularly coarse, and the actual effect depends on density and on how the outflow is dissipated within the host, it nevertheless implies that there could actually be a significant enrichment for a large stellar population and earlier for the ISM.

We have focused on low-luminosity quasars in the local Universe, characterized by relatively small black holes radiating near their Eddington limit. However, it is worth noting that the outflow phenomena are most prominent in the highest luminosity quasars. These super-luminous quasars exhibit a high prevalence of significant blueshifts in the blueshifts in the CIV $\lambda$ 1549 and [OIII] $\lambda\lambda$ 4959,5007 emission line profiles [39,40,112]. The ionized gas mass, kinetic energy, and mechanical thrust in these cases are remarkably high, implying extensive feedback effects on the host galaxies of these extremely luminous quasars. These effects were particularly pronounced during cosmic epochs of 2 to 6 billion years after the Big Bang, suggesting that these quasars might have played a substantial role in enriching the chemical composition of their host galaxies.

## 6. Discussion

### *A Gradient in Metal Content and Chemical Feedback along the Sequence*

A cartoon depicting a global evolutionary scenario is shown in Figure 6. At the one end of the sequence one encounters low mass, high Eddington ratio sources. They are accreting at a high rate, possibly following a merger and a burst of star formation. In the initial phases of the development of AGN and quasars, a series of events take place: wet mergers and strong interactions cause the accumulation of gas in the central regions of the galaxy. This accumulation triggers a burst of star formation (top of the inset) [113,114]. Over time, mass loss from stellar winds and supernova explosions provide a source of accretion fuel for the massive black hole located at the center of the galaxy. Subsequently, radiation force and mechanical energy can clear away the dust surrounding the black hole, particularly within a cone aligned with the axis of the accretion disk. This allows the radiative and mechanical energy to be released into the ISM of the host galaxy (bottom of the inset in Figure 6).

At a high accretion rate, a nuclear starburst can occur in the region where the disk becomes self-gravitating [115]. As mentioned, the  $Z$ -values calculated for the BLR of quasars appear exceptionally high when compared to their host galaxies. For reference, the highest measured  $Z$ -value in a molecular cloud is approximately five times the solar metallicity [78]. However, it is worth noting that the nuclear and circumnuclear environments of quasars can exhibit significant deviations from a typical interstellar setting. In these regions, stars traverse the disk, giving rise to the formation of accretion-modified objects that eventually attain substantial mass and, after a brief evolutionary phase, explode as core-collapse supernovae [115,116]. Stars within the nuclear vicinity can rapidly become highly massive (with masses exceeding 100 times the mass of the Sun), leading to core-collapse events that contribute to enriching the disk with heavy elements via the substantial metal yields

produced by supernova ejecta [80]. Furthermore, the compact remnants of these stars can continue accreting material, resulting in recurrent supernova occurrences [117]. These accretion-modified star formation processes that enhance metallicity are projected to yield metal abundances approximately in the range of 10 to 20 times solar metallicity [44], which aligns with the values observed in the xA sources.

At the other end of the sequence, one finds exceptionally massive black holes, radiating at low Eddington ratios, in conditions that are proximate to “starvation” and in any case to the exhaustion of the reservoir of gas for accretion. Accretion material can come from evolved stellar winds that can sustain modelled accretion rates [118]. Metallicity values might be in this case more conventional, around solar or subsolar, such as the values ranging from the order of 0.1 to approximately two times the solar metallicity found in the bulge of the Milky Way [119,120].

Population B sources have a slightly larger redshift than Pop. A (average  $z \approx 0.33$  versus 0.07) in quite a large Sloan Digital Sky Survey based low- $z$  sample [4] that might be straightforwardly explained by selection effects. However, a ten-fold increase in black hole mass from  $10^8 M_{\odot}$  at moderate accretion rate can occur over a time of about  $5 \times 10^8$  yr [10]. This timescale would correspond to a change in redshift  $\delta z \approx 0.05$ . Therefore, it is reasonable to assume that at least some Pop. B AGNs evolved from Pop. A sources locally.

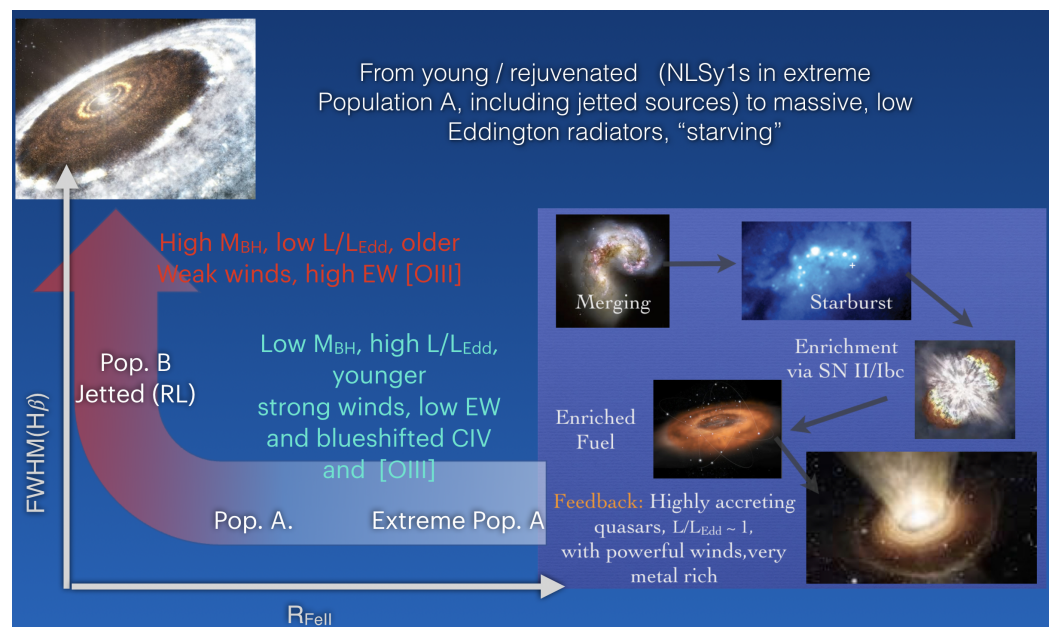


**Figure 6.** Sketch depicting the evolutionary interpretation of the quasar main sequence. The inset (right) shows a possible evolutionary path leading to highly accreting quasar showing evidence of high metal enrichment in the BLR.

### 7. Conclusions

In conclusion, the main sequence concept in quasars reveals a gradient of metallicity across different quasar populations, shedding light on their evolutionary paths. The understanding of these populations and their associated characteristics contributes to a deeper comprehension of the processes driving quasar behavior and their influence on their host galaxies. Expectations from accretion-modified stars within the active nuclei are consistent with highly supersolar metallicity.

**Author Contributions:** Conceptualization, P.M. and S.P.; methodology: P.M., M.S. and S.P.; formal analysis, P.M., S.P. and M.S.; Resources, D.D., A.D.O. and M.D.; data curation/analysis, A.F., K.G., M.S. and A.D.-M.; original draft preparation: P.M.; writing—review and editing: A.F., A.D.-M., M.S., S.P., M.D., E.B., N.B., A.D.O. and M.D.; funding acquisition, A.D.O. and D.D. All authors have read and agreed to the published version of the manuscript.

**Funding:** S.P. acknowledges the Conselho Nacional de Desenvolvimento Científico e Tecnológico (CNPq) Fellowships (164753/2020-6 and 313497/2022-2), Brazil. N.B. and E.B. acknowledge the support of the Serbian Ministry of Education, Science, and Technological Development, through the 695 contract number 451-03-68/2024-14/200002. A.d.O. and A.D.M. acknowledge financial support from the Spanish MCIU through project PID2022-140871NB-C21 by “ERDF A way of making Europe” and the Severo Ochoa grant CEX2021- 515001131-S funded by MCIN/AEI/10.13039/501100011033.

**Data Availability Statement:** Data are available from the corresponding author upon reasonable request.

**Conflicts of Interest:** The authors declare no conflict of interest.

### Abbreviations

The following abbreviations are used in this manuscript:

AGN	active galactic nuclei
A1,..., A4	Population A spectral types
BC	broad component
BLR	broad line region
BLUE	blueshifted component
B1, B2, B3	Population B spectral types
COS	Cosmic Origin Spectrograph
FIR	far-infrared
FOS	Faint Object Spectrograph
FWHM	full width at half maximum
HIL	high-ionization line
HST	Hubble Space Telescope
ISM	interstellar medium
LIL	low-ionization line
MAST	Mikulski Archive of Space Telescopes
Mrk	Markarian
MS	main sequence
NED	NASA/IPAC Extragalactic Database
NGC	New General Catalog
PHL	Palomar Haro Luyten
Pop.	Population
RL	radio-loud
RQ	radio-quiet
SED	spectral energy distribution
SOAR	Southern Observatory for Astrophysical Research
ST	spectral type
STIS	Space Telescope Imaging Spectrograph
UV	ultraviolet
VBC	very broad component
VBLR	very broad line region
xA	extreme Population A
Zw	Zwicky
4DE1	four-dimensional eigenvector 1

### References

1. Boroson, T.A.; Green, R.F. The Emission-Line Properties of Low-Redshift Quasi-stellar Objects. *Astrophys. J. Suppl.* **1992**, *80*, 109–135. [[CrossRef](#)]
2. Gaskell, C.M. Galactic Mergers, Starburst Galaxies, Quasar Activity and Massive Binary Black Holes. *Nature* **1985**, *315*, 386. [[CrossRef](#)]
3. Sulentic, J.W.; Zwitter, T.; Marziani, P.; Dultzin-Hacyan, D. Eigenvector 1: An Optimal Correlation Space for Active Galactic Nuclei. *Astrophys. J.* **2000**, *536*, L5–L9. [[CrossRef](#)]
4. Zamfir, S.; Sulentic, J.W.; Marziani, P.; Dultzin, D. Detailed Characterization of H $\beta$  Emission Line Profile in Low-z SDSS Quasars. *Mon. Not. R. Astron. Soc.* **2010**, *403*, 1759–1786. [[CrossRef](#)]
5. Shen, Y.; Ho, L.C. The Diversity of Quasars Unified by Accretion and Orientation. *Nature* **2014**, *513*, 210–213. [[CrossRef](#)] [[PubMed](#)]

6. Sun, J.; Shen, Y. Dissecting the Quasar Main Sequence: Insight from Host Galaxy Properties. *Astrophys. J. Lett.* **2015**, *804*, L15. [[CrossRef](#)]
7. Panda, S.; Marziani, P.; Czerny, B. The Quasar Main Sequence Explained by the Combination of Eddington Ratio, Metallicity, and Orientation. *Astrophys. J.* **2019**, *882*, 79. [[CrossRef](#)]
8. Giustini, M.; Proga, D. A Global View of the Inner Accretion and Ejection Flow Around Super Massive Black Holes. Radiation-driven Accretion Disk Winds in a Physical Context. *Astron. Astrophys.* **2019**, *630*, A94. [[CrossRef](#)]
9. Du, P.; et al. [SEAMBH Collaboration]. Supermassive Black Holes with High Accretion Rates in Active Galactic Nuclei. VI. Velocity-resolved Reverberation Mapping of the H $\beta$  Line. *Astrophys. J.* **2016**, *820*, 27. [[CrossRef](#)]
10. Fraix-Burnet, D.; Marziani, P.; D’Onofrio, M.; Dultzin, D. The Phylogeny of Quasars and the Ontogeny of Their Central Black Holes. *Front. Astron. Space Sci.* **2017**, *4*, 1. [[CrossRef](#)]
11. Panda, S. The CaFe Project: Optical Fe II and Near-Infrared Ca II Triplet Emission in Active Galaxies: Simulated EWs and the Co-dependence of Cloud Size and Metal Content. *Astron. Astrophys.* **2021**, *650*, A154. [[CrossRef](#)]
12. Hamann, F.; Ferland, G. The Chemical Evolution of QSOs and the Implications for Cosmology and Galaxy Formation. *Astrophys. J.* **1993**, *418*, 11–27. [[CrossRef](#)]
13. Nagao, T.; Marconi, A.; Maiolino, R. The Evolution of the Broad-Line Region among SDSS Quasars. *Astron. Astrophys.* **2006**, *447*, 157–172. [[CrossRef](#)]
14. Juarez, Y.; Maiolino, R.; Mujica, R.; Pedani, M.; Marinoni, S.; Nagao, T.; Marconi, A.; Oliva, E. The Metallicity of the Most Distant Quasars. *Astron. Astrophys.* **2009**, *494*, L25–L28. [[CrossRef](#)]
15. Matsuoka, K.; Nagao, T.; Marconi, A.; Maiolino, R.; Taniguchi, Y. The mass-metallicity relation of SDSS quasars. *Astron. Astrophys.* **2011**, *527*, A100. [[CrossRef](#)]
16. Shin, J.; Woo, J.H.; Nagao, T.; Kim, S.C. The Chemical Properties of Low-redshift QSOs. *Astrophys. J.* **2013**, *763*, 58. [[CrossRef](#)]
17. Sameshima, H.; Yoshii, Y.; Kawara, K. Chemical Evolution of the Universe at  $0.7 < z < 1.6$  Derived from Abundance Diagnostics of the Broad-Line Region of Quasars. *Astrophys. J.* **2017**, *834*, 203. [[CrossRef](#)]
18. Wang, S.; Jiang, L.; Shen, Y.; Ho, L.C.; Vestergaard, M.; Bañados, E.; Willott, C.J.; Wu, J.; Zou, S.; Yang, J.; et al. Metallicity in Quasar Broad-Line Regions at Redshift 6. *Astrophys. J.* **2022**, *925*, 121. [[CrossRef](#)]
19. Matteucci, F. *Chemical Evolution of Galaxies*; Springer: Berlin/Heidelberg, Germany, 2012. [[CrossRef](#)]
20. Xu, F.; Bian, F.; Shen, Y.; Zuo, W.; Fan, X.; Zhu, Z. The Evolution of Chemical Abundance in Quasar Broad Line Region. *Mon. Not. R. Astron. Soc.* **2018**, *480*, 345–357. [[CrossRef](#)]
21. Marziani, P.; Panda, S.; Deconto Machado, A.; Del Olmo, A. Metal Content in Relativistically Jetted and Radio-Quiet Quasars in the Main Sequence Context. *Galaxies* **2023**, *11*, 52. [[CrossRef](#)]
22. Śniegowska, M.; Marziani, P.; Czerny, B.; Panda, S.; Martínez-Aldama, M.L.; del Olmo, A.; D’Onofrio, M. High Metal Content of Highly Accreting Quasars. *Astrophys. J.* **2021**, *910*, 115. [[CrossRef](#)]
23. Di Matteo, T.; Springel, V.; Hernquist, L. Energy Input from Quasars Regulates the Growth and Activity of Black Holes and Their Host Galaxies. *Nature* **2005**, *433*, 604–607. [[CrossRef](#)]
24. Hopkins, P.F.; Hernquist, L.; Cox, T.J.; Di Matteo, T.; Robertson, B.; Springel, V. A Unified, Merger-driven Model of the Origin of Starbursts, Quasars, the Cosmic X-Ray Background, Supermassive Black Holes, and Galaxy Spheroids. *Astrophys. J. Suppl.* **2006**, *163*, 1–49. [[CrossRef](#)]
25. Somerville, R.S.; Davé, R. Physical Models of Galaxy Formation in a Cosmological Framework. *Annu. Rev. Astron. Astrophys.* **2015**, *53*, 51–113. [[CrossRef](#)]
26. Marziani, P.; Sulentic, J.W.; Zamanov, R.; Calvani, M.; Dultzin-Hacyan, D.; Bachev, R.; Zwitter, T. An Optical Spectroscopic Atlas of Low-Redshift Active Galactic Nuclei. *Astrophys. J. Suppl.* **2003**, *145*, 199–211. [[CrossRef](#)]
27. Punsly, B.; Marziani, P.; Bennert, V.N.; Nagai, H.; Gurwell, M.A. Revealing the Broad Line Region of NGC 1275: The Relationship to Jet Power. *Astrophys. J.* **2018**, *869*, 143. [[CrossRef](#)]
28. Marinello, M.; Rodríguez-Ardila, A.; Marziani, P.; Sigut, A.; Pradhan, A. Panchromatic Properties of the Extreme Fe II Emitter PHL 1092. *Mon. Not. R. Astron. Soc.* **2020**, *494*, 4187–4202. [[CrossRef](#)]
29. Garnica, K.; Negrete, C.A.; Marziani, P.; Dultzin, D.; Śniegowska, M.; Panda, S. High Metal Content of Highly Accreting Quasars: Analysis of an Extended Sample. *Astron. Astrophys.* **2022**, *667*, A105. [[CrossRef](#)]
30. Collin-Souffrin, S.; Dyson, J.E.; McDowell, J.C.; Perry, J.J. The Environment of Active Galactic Nuclei. I—A Two-component Broad Emission Line Model. *Mon. Not. R. Astron. Soc.* **1988**, *232*, 539–550. [[CrossRef](#)]
31. Elvis, M. A Structure for Quasars. *Astrophys. J.* **2000**, *545*, 63–76. [[CrossRef](#)]
32. Peterson, B.M.; Wandel, A. Keplerian Motion of Broad-Line Region Gas as Evidence for Supermassive Black Holes in Active Galactic Nuclei. *Astrophys. J. Lett.* **1999**, *521*, L95–L98. [[CrossRef](#)]
33. Peterson, B.M.; Wandel, A. Evidence for Supermassive Black Holes in Active Galactic Nuclei from Emission-Line Reverberation. *Astrophys. J. Lett.* **2000**, *540*, L13–L16. [[CrossRef](#)]
34. Richards, G.T.; Kruczek, N.E.; Gallagher, S.C.; Hall, P.B.; Hewett, P.C.; Leighly, K.M.; Deo, R.P.; Kratzer, R.M.; Shen, Y. Unification of Luminous Type 1 Quasars through C IV Emission. *Astron. J.* **2011**, *141*, 167. [[CrossRef](#)]
35. Coatman, L.; Hewett, P.C.; Banerji, M.; Richards, G.T. C IV Emission-Line Properties and Systematic Trends in Quasar Black Hole Mass Estimates. *Mon. Not. R. Astron. Soc.* **2016**, *461*, 647–665. [[CrossRef](#)]

36. Ferland, G.J.; Hu, C.; Wang, J.; Baldwin, J.A.; Porter, R.L.; van Hoof, P.A.M.; Williams, R.J.R. Implications of Infalling Fe II-Emitting Clouds in Active Galactic Nuclei: Anisotropic Properties. *Astrophys. J. Lett.* **2009**, *707*, L82–L86. [[CrossRef](#)]
37. Véron-Cetty, M.P.; Véron, P.; Gonçalves, A.C. A Spectrophotometric Atlas of Narrow-Line Seyfert 1 galaxies. *Astron. Astrophys.* **2001**, *372*, 730–754. [[CrossRef](#)]
38. Marziani, P.; Negrete, C.A.; Dultzin, D.; Martínez-Aldama, M.L.; Del Olmo, A.; D’Onofrio, M.; Stirpe, G.M. Quasar Massive Ionized Outflows Traced by CIV  $\lambda 1549$  and [OIII] $\lambda\lambda 4959,5007$ . *Front. Astron. Space Sci.* **2017**, *4*, 16. [[CrossRef](#)]
39. Vietri, G.; Piconcelli, E.; Bischetti, M.; Duras, F.; Martocchia, S.; Bongiorno, A.; Marconi, A.; Zappacosta, L.; Bisogni, S.; Bruni, G.; et al. The WISSH Quasars Project. IV. Broad Line Region versus Kiloparsec-scale Winds. *Astron. Astrophys.* **2018**, *617*, A81. [[CrossRef](#)]
40. Deconto-Machado, A.; del Olmo Orozco, A.; Marziani, P.; Perea, J.; Stirpe, G.M. High-Redshift Quasars along the Main Sequence. *Astron. Astrophys.* **2023**, *669*, A83. [[CrossRef](#)]
41. Leighly, K.M.; Moore, J.R. *Hubble Space Telescope* STIS Ultraviolet Spectral Evidence of Outflow in Extreme Narrow-Line Seyfert 1 Galaxies. I. Data and Analysis. *Astrophys. J.* **2004**, *611*, 107–124. [[CrossRef](#)]
42. Mejía-Restrepo, J.E.; Trakhtenbrot, B.; Lira, P.; Netzer, H.; Capellupo, D.M. Active Galactic Nuclei at  $z \sim 1.5$ —II. Black Hole Mass Estimation by Means of Broad Emission Lines. *Mon. Not. R. Astron. Soc.* **2016**, *460*, 187–211. [[CrossRef](#)]
43. Vietri, G.; Mainieri, V.; Kakkad, D.; Netzer, H.; Perna, M.; Circosta, C.; Harrison, C.M.; Zappacosta, L.; Husemann, B.; Padovani, P.; et al. SUPER. III. Broad Line Region Properties of AGNs at  $z \sim 2$ . *Astron. Astrophys.* **2020**, *644*, A175. [[CrossRef](#)]
44. Wang, H.; Wang, T.; Zhou, H.; Liu, B.; Wang, J.; Yuan, W.; Dong, X. Coexistence of Gravitationally-bound and Radiation-driven C IV Emission Line Regions in Active Galactic Nuclei. *Astrophys. J.* **2011**, *738*, 85. [[CrossRef](#)]
45. Marconi, A.; Axon, D.J.; Maiolino, R.; Nagao, T.; Pietrini, P.; Risaliti, G.; Robinson, A.; Torricelli, G. On the Observed Distributions of Black Hole Masses and Eddington Ratios from Radiation Pressure Corrected Virial Indicators. *Astrophys. J. Lett.* **2009**, *698*, L103–L107. [[CrossRef](#)]
46. Wang, J.; Wei, J.Y.; He, X.T. A Sample of IRAS Infrared-selected Seyfert 1.5 Galaxies: Infrared Color  $\alpha(60, 25)$ -dominated Eigenvector 1. *Astrophys. J.* **2006**, *638*, 106–119. [[CrossRef](#)]
47. Wolf, J.; Salvato, M.; Coffey, D.; Merloni, A.; Buchner, J.; Arcodia, R.; Baron, D.; Carrera, F.J.; Comparat, J.; Schneider, D.P.; et al. Exploring the Diversity of Type 1 Active Galactic Nuclei Identified in SDSS-IV/SPIDERS. *Mon. Not. R. Astron. Soc.* **2020**, *492*, 3580–3601. [[CrossRef](#)]
48. Peterson, B.M.; Ferland, G.J. An Accretion Event in the Seyfert Galaxy NGC 5548. *Nature* **1986**, *324*, 345–347. [[CrossRef](#)]
49. Snedden, S.; Gaskell, C. Different Velocity Dependences of Physical Conditions of High- and Low-Ionization Lines in Broad-Line Regions. In *AGN Physics with the Sloan Digital Sky Survey*; Richards, G.T., Hall, P.B., Eds.; Astronomical Society of the Pacific: San Francisco, CA, USA, 2004; pp. 197–200. Available online: <http://aspbooks.org/custom/publications/paper/311-0197.html> (accessed on 7 January 2024).
50. Morris, S.L.; Ward, M.J. Optically Thin Gas in the Broad-line Region of Seyfert Galaxies. *Astrophys. J.* **1989**, *340*, 713–728. [[CrossRef](#)]
51. Netzer, H. On the Profiles of the Broad Lines in the Spectra of QSOs and Seyfert Galaxies. *Mon. Not. R. Astron. Soc.* **1977**, *181*, 89P–92P. [[CrossRef](#)]
52. Corbin, M.R. QSO Broad Emission Line Asymmetries: Evidence of Gravitational Redshift? *Astrophys. J.* **1995**, *447*, 496–504. [[CrossRef](#)]
53. Popovič, L.Č.; Vince, I.; Atanacković-Vukmanović, O.; Kubičela, A. Contribution of Gravitational Redshift to Spectral Line Profiles of Seyfert Galaxies and Quasars. *Astron. Astrophys.* **1995**, *293*, 309–314. Available online: <https://ui.adsabs.harvard.edu/abs/1995A%2526A...293..309P/> (accessed on 7 January 2024).
54. Muñoz, J.A.; Falco, E.E.; Kochanek, C.S.; Lehár, J.; Mediavilla, E. The Redshift Distribution of Flat-Spectrum Radio Sources. *Astrophys. J.* **2003**, *594*, 684–694. [[CrossRef](#)]
55. Mediavilla, E.; Jiménez-Vicente, J.; Fian, C.; Muñoz, J.A.; Falco, E.; Motta, V.; Guerras, E. Systematic Redshift of the Fe III UV Lines in Quasars: Measuring Supermassive Black Hole Masses under the Gravitational Redshift Hypothesis. *Astrophys. J.* **2018**, *862*, 104. [[CrossRef](#)]
56. Fian, C.; Mediavilla, E.; Jiménez-Vicente, J.; Motta, V.; Muñoz, J.A.; Chelouche, D.; Hanslmeier, A. Revealing the Structure of the Lensed Quasar Q 0957+561. II. Supermassive Black Hole Mass via Gravitational Redshift. *Astron. Astrophys.* **2022**, *667*, A67. [[CrossRef](#)]
57. Wang, J.-M.; et al. [SEAMBH Collaboration]. Supermassive Black Holes with High Accretion Rates in Active Galactic Nuclei. II. The Most Luminous Standard Candles in the Universe. *Astrophys. J.* **2014**, *793*, 108. [[CrossRef](#)]
58. Marziani, P. Accretion/Ejection Phenomena and Emission-Line Profile (A)symmetries in Type-1 Active Galactic Nuclei. *Symmetry* **2023**, *15*, 1859. [[CrossRef](#)]
59. Pagel, B.E.J.; Edmunds, M.G.; Blackwell, D.E.; Chun, M.S.; Smith, G. On the Composition of H II Regions in Southern Galaxies—I. NGC 300 and 1365. *Mon. Not. R. Astron. Soc.* **1979**, *189*, 95–113. [[CrossRef](#)]
60. Huang, J.; Lin, D.N.C.; Shields, G. Metal Enrichment Due to Embedded Stars in AGN Discs. *Mon. Not. R. Astron. Soc.* **2023**, *525*, 5702–5718. [[CrossRef](#)]
61. Ferland, G.J.; Baldwin, J.A.; Korista, K.T.; Hamann, F.; Carswell, R.F.; Phillips, M.; Wilkes, B.; Williams, R.E. High Metal Enrichments in Luminous Quasars. *Astrophys. J.* **1996**, *461*, 683–697. [[CrossRef](#)]

62. Hamann, F.; Korista, K.T.; Ferland, G.J.; Warner, C.; Baldwin, J. Metallicities and Abundance Ratios from Quasar Broad Emission Lines. *Astrophys. J.* **2002**, *564*, 592–603. [CrossRef]
63. Osmer, P.S.; Smith, M.G. The Emission-Line Spectra of Nine Newly Discovered, Optically Selected Quasars with Redshift 2.5 to 3.1. *Astrophys. J.* **1976**, *210*, 267–276. [CrossRef]
64. Shields, G.A. The abundance of nitrogen in QSOs. *Astrophys. J.* **1976**, *204*, 330–336. [CrossRef]
65. Vila-Costas, M.B.; Edmunds, M.G. The Nitrogen-to-Oxygen Ratio in Galaxies and Its Implications for the Origin of nitrogen. *Mon. Not. R. Astron. Soc.* **1993**, *265*, 199–212. [CrossRef]
66. Izotov, Y.I.; Thuan, T.X. Heavy-Element Abundances in Blue Compact Galaxies. *Astrophys. J.* **1999**, *511*, 639–659. [CrossRef]
67. Collin, S.; Joly, M. The Fe II Problem in NLS1s. *New Astron. Rev.* **2000**, *44*, 531–537. [CrossRef]
68. Matsuoka, Y.; Kawara, K.; Oyabu, S. Low-Ionization Emission Regions in Quasars: Gas Properties Probed with Broad O I and Ca II Lines. *ApJ* **2008**, *673*, 62–68. [CrossRef]
69. Ferland, G.J.; Chatzikos, M.; Guzmán, F.; Lykins, M.L.; van Hoof, P.A.M.; Williams, R.J.R.; Abel, N.P.; Badnell, N.R.; Keenan, F.P.; Porter, R.L.; et al. The 2017 Release Cloudy. *Rev. Mex. Astronom. Astrofis.* **2017**, *53*, 385–438. Available online: <https://www.astroscu.unam.mx/RMxAA/vol53.html> (accessed on 7 January 2024).
70. Baldwin, J.; Ferland, G.; Korista, K.; Verner, D. Locally Optimally Emitting Clouds and the Origin of Quasar Emission Lines. *Astrophys. J.* **1995**, *455*, L119–L122. [CrossRef]
71. Korista, K.; Baldwin, J.; Ferland, G.; Verner, D. An Atlas of Computed Equivalent Widths of Quasar Broad Emission Lines. *Astrophys. J. Suppl.* **1997**, *108*, 401–415. [CrossRef]
72. Mathews, W.G.; Ferland, G.J. What Heats the Hot Phase in Active Nuclei? *Astrophys. J.* **1987**, *323*, 456–467. [CrossRef]
73. Ferland, G.J.; Done, C.; Jin, C.; Landt, H.; Ward, M.J. State-of-the-Art AGN SEDs for Photoionization Models: BLR Predictions Confront the Observations. *Mon. Not. R. Astron. Soc.* **2020**, *494*, 5917–5922. [CrossRef]
74. Sigut, T.A.A.; Pradhan, A.K. Ly alpha Fluorescent Excitation of Fe II in Active Galactic Nuclei. *Astrophys. J.* **1998**, *499*, L139–L142. [CrossRef]
75. Sigut, T.A.A.; Pradhan, A.K. Predicted Fe II Emission-Line Strengths from Active Galactic Nuclei. *Astrophys. J. Suppl.* **2003**, *145*, 15–37. [CrossRef]
76. D’Agostini, G. *Bayesian Reasoning in Data Analysis: A Critical Introduction*; World Scientific: Singapore, 2003. [CrossRef]
77. Nagao, T.; Maiolino, R.; Marconi, A. Gas Metallicity in the Narrow-Line Regions of High-Redshift Active Galactic Nuclei. *Astron. Astrophys.* **2006**, *447*, 863–876. [CrossRef]
78. Maiolino, R.; Mannucci, F. De re Metallica: The Cosmic Chemical Evolution of Galaxies. *Astron. Astrophys. Rev.* **2019**, *27*, 3. [CrossRef]
79. Wang, J.M.; Songsheng, Y.Y.; Li, Y.R.; Du, P. Final Stage of Merging Binaries of Supermassive Black Holes: Observational Signatures. *Mon. Not. R. Astron. Soc.* **2023**, *518*, 3397–3406. [CrossRef]
80. Cantiello, M.; Jermyn, A.S.; Lin, D.N.C. Stellar Evolution in AGN Disks. *Astrophys. J.* **2021**, *910*, 94. [CrossRef]
81. Heckman, T.M.; Baum, S.A.; van Breugel, W.J.M.; McCarthy, P. Dynamical, Physical, and Chemical Properties of Emission-Line Nebulae in Cooling Flows. *Astrophys. J.* **1989**, *338*, 48–77. [CrossRef]
82. Lim, J.; Ao, Y.; Dinh-V-Trung. Radially Inflowing Molecular Gas in NGC 1275 Deposited by an X-Ray Cooling Flow in the Perseus Cluster. *Astrophys. J.* **2008**, *672*, 252–265. [CrossRef]
83. Sun, W.H.; Malkan, M.A. Fitting Improved Accretion Disk Models to the Multiwavelength Continua of Quasars and Active Galactic Nuclei. *Astrophys. J.* **1989**, *346*, 68–100. [CrossRef]
84. Sulentic, J.W.; Bachev, R.; Marziani, P.; Negrete, C.A.; Dultzin, D. C IV  $\lambda$ 1549 as an Eigenvector 1 Parameter for Active Galactic Nuclei. *Astrophys. J.* **2007**, *666*, 757–777. [CrossRef]
85. Mauch, T.; Murphy, T.; Buttery, H.J.; Curran, J.; Hunstead, R.W.; Piestrzynski, B.; Robertson, J.G.; Sadler, E.M. SUMSS: A Wide-Field Radio Imaging Survey of the Southern Sky—II. The Source Catalogue. *Mon. Not. R. Astron. Soc.* **2003**, *342*, 1117–1130. [CrossRef]
86. Sikora, M.; Stawarz, Ł.; Lasota, J.P. Radio Loudness of Active Galactic Nuclei: Observational Facts and Theoretical Implications. *Astrophys. J.* **2007**, *658*, 815–828. [CrossRef]
87. Peterson, B.M.; Ferrarese, L.; Gilbert, K.M.; Kaspi, S.; Malkan, M.A.; Maoz, D.; Merritt, D.; Netzer, H.; Onken, C.A.; Pogge, R.W.; et al. Central Masses and Broad-Line Region Sizes of Active Galactic Nuclei. II. A Homogeneous Analysis of a Large Reverberation-Mapping Database. *Astrophys. J.* **2004**, *613*, 682–699. [CrossRef]
88. Bentz, M.C.; Katz, S. The AGN Black Hole Mass Database. *Publ. Astron. Soc. Pacif.* **2015**, *127*, 67–73. [CrossRef]
89. Jiang, B.W.; Marziani, P.; Savić, Đ.; Shablovinskaya, E.; Popović, L.Č.; Afanasiev, V.L.; Czerny, B.; Wang, J.M.; del Olmo, A.; D’Onofrio, M.; et al. Linear Spectropolarimetric Analysis of Fairall 9 with VLT/FORS2. *Mon. Not. R. Astron. Soc.* **2021**, *508*, 79–99. [CrossRef]
90. Buendia-Rios, T.M.; Negrete, C.A.; Marziani, P.; Dultzin, D. Statistical Analysis of Al III and C III] Emission Lines as Virial Black Hole Mass Estimators in Quasars. *Astron. Astrophys.* **2023**, *669*, A135. [CrossRef]
91. Marshall, H.L.; Carone, T.E.; Shull, J.M.; Malkan, M.A.; Elvis, M. The Steep Soft X-Ray Spectrum of the Highly Variable Active Nucleus in Markarian 478. *Astrophys. J.* **1996**, *457*, 169–176. [CrossRef]
92. Hwang, C.Y.; Bowyer, S. The Extreme-Ultraviolet Emission of the Seyfert Galaxies Markarian 279, Markarian 478, and Ton S180. *Astrophys. J.* **1997**, *475*, 552–556. [CrossRef]

93. Yuan, Q.; Brotherton, M.; Green, R.F.; Kriss, G.A. Outflowing Components in the Prototype Narrow-Line Seyfert 1 Galaxy Markarian 478. In *Recycling Intergalactic and Interstellar Matter*; Duc, P.-A., Braine, J., Brinks, E., Eds.; Astronomical Society of the Pacific: San Francisco, CA, USA, 2004; pp. 364–365. Available online: <https://ui.adsabs.harvard.edu/abs/2004IAUS..217..364Y/> (accessed on 7 January 2024).
94. Zacharias, N.; Monet, D.G.; Levine, S.E.; Urban, S.E.; Gaume, R.; Wycoff, G.L. VizieR Online Data Catalog: NOMAD Catalog (Zacharias+ 2005). *VizieR Online Data Catalog* **2005**, I/297. Available online: <https://cdsarc.cds.unistra.fr/viz-bin/cat/I/297> (accessed on 7 January 2024).
95. Vestergaard, M. A First Step Toward Constraining Supermassive Black-Hole Growth. *New Astron. Rev.* **2006**, *50*, 817–820. [[CrossRef](#)]
96. Kellermann, K.I.; Sramek, R.; Schmidt, M.; Shaffer, D.B.; Green, R. VLA observations of objects in the Palomar Bright Quasar Survey. *Astron. J.* **1989**, *98*, 1195–1207. [[CrossRef](#)]
97. Popović, L.Č.; Mediavilla, E.; Bon, E.; Ilić, D. Contribution of the Disk Emission to the Broad Emission Lines in AGNs: Two-component Model. *Astron. Astrophys.* **2004**, *423*, 909–918. [[CrossRef](#)]
98. Snedden, S.A.; Gaskell, C.M. The Case for Optically Thick High-Velocity Broad-Line Region Gas in Active Galactic Nuclei. *Astrophys. J.* **2007**, *669*, 126–134. [[CrossRef](#)]
99. Bon, E.; Gavrilović, N.; La Mura, G.; Popović, L.Č. Complex Broad Emission Line Profiles of AGN—Geometry of the Broad Line Region. *New Astron. Rev.* **2009**, *53*, 121–127. [[CrossRef](#)]
100. Vietri, G. The LBT/WISSH Quasar Survey: Revealing Ultra-Massive Black Holes and Powerful Winds in the Most Luminous Quasars. Talk at the Durham-Dartmouth Extragalactic Workshop *Are AGN Special?* Durham, UK, 30 July–3 August 2018. Available online: [http://astro.dur.ac.uk/Are\\_AGN\\_Special/presentations.php](http://astro.dur.ac.uk/Are_AGN_Special/presentations.php) (accessed on 7 January 2024).
101. Yang, J.; Wang, F.; Fan, X.; Hennawi, J.F.; Barth, A.J.; Bañados, E.; Sun, F.; Liu, W.; Cai, Z.; Jiang, L.; et al. A Spectroscopic Survey of Biased Halos in the Reionization Era (ASPIRE): A First Look at the Rest-frame Optical Spectra of  $z > 6.5$  Quasars Using JWST. *Astrophys. J. Lett.* **2023**, *951*, L5. [[CrossRef](#)]
102. Shang, Z.; Wills, B.J.; Wills, D.; Brotherton, M.S. Spectral Properties from Ly $\alpha$  to H $\alpha$  for an Essentially Complete Sample of Quasars. I. Data. *Astron. J.* **2007**, *134*, 294–393. [[CrossRef](#)]
103. Azzalini, A.; Regoli, G. Some Properties of Skew-Symmetric Distributions. *Ann. Inst. Statist. Math.* **2012**, *64*, 857–879. [[CrossRef](#)]
104. Marziani, P.; Sulentic, J.W.; Plauchu-Frayn, I.; del Olmo, A. Is MgII $\lambda$ 2800 a Reliable Virial Broadening Estimator for Quasars? *Astron. Astrophys.* **2013**, *555*, A89. [[CrossRef](#)]
105. Feruglio, C.; Maiolino, R.; Piconcelli, E.; Menci, N.; Aussel, H.; Lamastra, A.; Fiore, F. Quasar Feedback Revealed by Giant Molecular Outflows. *Astron. Astrophys.* **2010**, *518*, L155. [[CrossRef](#)]
106. Harrison, C.M.; Alexander, D.M.; Mullaney, J.R.; Swinbank, A.M. Kiloparsec-scale Outflows are Prevalent Among Luminous AGN: Outflows and Feedback in the Context of the Overall AGN Population. *Mon. Not. R. Astron. Soc.* **2014**, *441*, 3306–3347. [[CrossRef](#)]
107. Feruglio, C.; Fiore, F.; Carniani, S.; Piconcelli, E.; Zappacosta, L.; Bongiorno, A.; Cicone, C.; Maiolino, R.; Marconi, A.; Menci, N.; et al. The Multi-phase Winds of Markarian 231: From the Hot, Nuclear, Ultra-fast Wind to the Galaxy-scale, Molecular Outflow. *Astron. Astrophys.* **2015**, *583*, A99. [[CrossRef](#)]
108. Woo, J.-H.; Bae, H.-J.; Son, D.; Karouzos, M. The Prevalence of Gas Outflows in Type 2 AGNs. *Astrophys. J.* **2016**, *817*, 108. [[CrossRef](#)]
109. Kovačević-Dojčinović, J.; Dojčinović, I.; Lakićević, M.; Popović, L.Č. Tracing the Outflow Kinematics in Type 2 Active Galactic Nuclei. *Astron. Astrophys.* **2022**, *659*, A130. [[CrossRef](#)]
110. Collin, S.; Boisson, C.; Mouchet, M.; Dumont, A.M.; Coupé, S.; Porquet, D.; Rokaki, E. Are Quasars Accreting at Super-Eddington Rates? *Astron. Astrophys.* **2002**, *388*, 771–786. [[CrossRef](#)]
111. Li, L.-X. Accretion, Growth of Supermassive Black Holes, and Feedback in Galaxy Mergers. *Mon. Not. R. Astron. Soc.* **2012**, *424*, 1461–1470. [[CrossRef](#)]
112. Bischetti, M.; Piconcelli, E.; Vietri, G.; Bongiorno, A.; Fiore, F.; Sani, E.; Marconi, A.; Duras, F.; Zappacosta, L.; Brusa, M.; et al. The WISSH Quasars Project. I. Powerful Ionised Outflows in Hyper-Luminous Quasars. *Astron. Astrophys.* **2017**, *598*, A122. [[CrossRef](#)]
113. Sanders, D.B.; Soifer, B.T.; Elias, J.H.; Madore, B.F.; Matthews, K.; Neugebauer, G.; Scoville, N.Z. Ultraluminous Infrared Galaxies and the Origin of Quasars. *Astrophys. J.* **1988**, *325*, 74–91. [[CrossRef](#)]
114. Sanders, D.B.; Kartaltepe, J.S.; Kewley, L.J.; U, V.; Yuan, T.; Evans, A.S.; Armus, L.; Mazzarella, J.M. Luminous Infrared Galaxies and the “Starburst-AGN Connection”. In *The Starburst-AGN Connection*; Wang, W., Yang, Z., Luo, Z., Chen, Z., Eds.; Astronomical Society of the Pacific: San Francisco, CA, USA, 2009; pp. 3–13. Available online: [http://aspbooks.org/a/volumes/article\\_details/?paper\\_id=30188](http://aspbooks.org/a/volumes/article_details/?paper_id=30188) (accessed on 7 January 2024).
115. Collin, S.; Zahn, J.-P. Star Formation and Evolution in Accretion Disks around Massive Black Holes. *Astron. Astrophys.* **1999**, *344*, 433–449. Available online: <https://ui.adsabs.harvard.edu/abs/1999A%26A...344..433C/> (accessed on 7 January 2024).
116. Cheng, K.S.; Wang, J.-M. The Formation and Merger of Compact Objects in the Central Engine of Active Galactic Nuclei and Quasars: Gamma-Ray Burst and Gravitational Radiation. *Astrophys. J.* **1999**, *521*, 502–508. [[CrossRef](#)]

117. Lin, D.N.C. Star/Disk Interaction in the Nuclei of Active Galaxies. In *Emission Lines in Active Galaxies: New Methods and Techniques*; Peterson, B.M., Cheng, F.Z., Wilson, A.S., Eds.; Astronomical Society of the Pacific: San Francisco, CA, USA, 1997; pp. 64–65. Available online: [http://aspbooks.org/a/volumes/article\\_details/?paper\\_id=13558](http://aspbooks.org/a/volumes/article_details/?paper_id=13558) (accessed on 7 January 2024).
118. Padovani, P.; Matteucci, F. Stellar Mass Loss in Elliptical Galaxies and the Fueling of Active Galactic Nuclei. *Astrophys. J.* **1993**, *416*, 26–35. [[CrossRef](#)]
119. Zoccali, M.; Renzini, A.; Ortolani, S.; Greggio, L.; Saviane, I.; Cassisi, S.; Rejkuba, M.; Barbuy, B.; Rich, R.M.; Bica, E. Age and Metallicity Distribution of the Galactic Bulge from Extensive Optical and Near-IR Stellar Photometry. *Astron. Astrophys.* **2003**, *399*, 931–956. [[CrossRef](#)]
120. Gonzalez, O.A.; Gadotti, D. The Milky Way Bulge: Observed Properties and a Comparison to External Galaxies. In *Galactic Bulges*; Laurikainen, E., Peletier, R., Gadotti, D., Eds.; Springer International Publishing Switzerland: Cham, Switzerland, 2016; pp. 199–232. [[CrossRef](#)]

**Disclaimer/Publisher’s Note:** The statements, opinions and data contained in all publications are solely those of the individual author(s) and contributor(s) and not of MDPI and/or the editor(s). MDPI and/or the editor(s) disclaim responsibility for any injury to people or property resulting from any ideas, methods, instructions or products referred to in the content.